Journal of Constructional Steel Research 235 (2025) 109776

Contents lists available at ScienceDirect

Journal of Constructional Steel Research

journal homepage: www.elsevier.com/locate/jcsr

Experimental and numerical investigation on hysteretic behavior of steel grid shear walls

Alireza Vatankhah, Abbas Karamodin *

Department of Civil Engineering, Faculty of Engineering, Ferdowsi University of Mashhad, Mashhad, Iran

ARTICLE INFO

Keywords:
Steel grid shear wall
Quasi-static loading
Steel plate shear wall
Finite element analysis
Initial stiffness
Response modification factor

ABSTRACT

Steel plate shear walls have emerged as a promising lateral load-resisting system in tall buildings, owing to their high lateral resistance, ductility, and cost-effectiveness. However, they encounter challenges such as imposing significant stresses on surrounding elements and lacking versatility in accommodating different uses. To address these issues, researchers have proposed various solutions, including stiffened steel plate shear walls and shear walls with different types of openings. In this paper, a new lateral resisting system, the steel grid shear wall (SGSW), has been introduced to overcome these limitations. Also this paper presents an experimental and numerical investigation of a novel SGSW under quasi-static loading. A SGSW specimen was tested, demonstrating desirable yielding and failure processes. Furthermore, the finite element model of SGSW was validated against experimental results, exhibiting high accuracy. The SGSW specimen displayed stable hysteretic behavior, high ductility, substantial shear strength, and energy dissipation capacity. Moreover, it showed a higher initial stiffness and ductility reduction factor compared to an equivalent steel plate shear wall. The proposed SGSW system presents a viable alternative for lateral load resistance in buildings, offering advantages such as ease of implementation, cost-effectiveness, and stable hysteretic performance.

1. Introduction

Undoubtedly, in consideration of their height, all structures necessitate a resilient lateral load-bearing system to counteract the loads caused by wind and earthquakes. In recent years, the utilization of steel plate shear walls has garnered attention as a modern lateral load-resisting system in tall buildings due to their high lateral resistance, ductility, significant energy dissipation capacity, cost-effectiveness, and shorter construction time. Despite thementioned advantages, steel plate shear walls have some drawbacks. These include the imposition of substantial stresses on surrounding components due to the post-buckling behavior of the steel plate, the inability to accommodate utilities within the wall cavity, and compression buckling of the hystersis curves resulting from out-of-plane bending of the plate.

Takahashi et al. [1] conducted the first comprehensive study on full-scale stiffened steel shear walls. Their research showed that the inclusion of stiffeners effectively controls out-of-plane buckling and improves the energy dissipation capacity of the system. Additionally, previous investigations by researchers [2–7]. have indicated that the lateral resistance in the steel plate shear wall system is due to the post-buckling resistance of the plate and the development of a tensile field within it. In light of these findings, researchers aimed to develop a simple and accurate method for analyzing and designing such systems. Consequently, Thorburn et al. [8] proposed the Strip Model as a means to estimate the forces imposed on the surrounding frame due to the yielding of the steel plate. This model disregards the compressive strength of the plate and attributes the system's resistance solely to the formation of a tensile field within the web plate. Furthermore, Timler and Kulak [9] evaluated the accuracy of the Strip Model through a full-scale experiment and proposed equations for calculating the angles at which tensile fields form, taking into account the stiffness of the surrounding elements. Numerous studies have been conducted by researchers [10–12] have aimed to enhance the accuracy of these equations. Collectively, these investigations demonstrate that the Strip Model exhibits strong predictive capabilities for the mechanical performance of steel plate shear walls. Furthermore, multiple types of steel shear walls have been developed by researchers to enhance energy dissipation capacity, lateral resistance, and reduce hysteresis loop degradation. Experimental studies have been conducted to investigate the performance of these developed systems. Among the methods proposed by researchers to control out-of-plane

* Corresponding author.
E-mail addresses: alireza.vatankhah@alumni.um.ac.ir (A. Vatankhah), a-karam@um.ac.ir (A. Karamodin).

https://doi.org/10.1016/j.jcsr.2025.109776
Received 6 March 2025; Received in revised form 20 June 2025; Accepted 29 June 2025
Available online 19 July 2025

buckling, the use of stiffened steel plate shear walls has been suggested. In this approach, the installation of stiffeners helps increase the shear capacity of the plate, enhance energy absorption capacity, and improve the seismic performance of the system [13,14,23–25,15–22].

However, this solution suffers from certain drawbacks, including high cost, time-consuming implementation, rigorous precision requirements, and the possibility of steel plate buckling during the welding process due to its very thin thickness.Another limitation of SPSWs is their inability to accommodate utilities in areas where plates are present. To address this issue, various types of steel shear walls with openings have been developed and tested. To this end, after conducting an experimental study, two patterns of creating openings in steel shear walls were proposed by Vian et al. [26]. Subsequently, based on the results obtained from this research, a relationship to calculate the shear resistance of perforated steel shear walls was proposed by Purba and Bruneau [27]. Moreover, researchers have numerically and experimentally studied the behavior of SPSWs with different openings, and relationships have been proposed to estimate the shear resistance of such panels [14,26,28–33].

Due to limitations in accessing steel sheets with very thin thickness and the prevention of project uneconomicalization due to the use of thicker sheets than necessary for design, solutions have been proposed by researchers. Among these methods, the use of perforated shear panels, steel sheets with low yield stress [34–36], different groove patterns in steel sheets [37–42], various connection modes of shear panels to surrounding frames [43–47], and the use of shear panels with different patterns of interface elements [48–54] can be mentioned. However, using these methods entails limitations such as the generation of steel waste due to creating holes in the sheet and the lack of quick access to LYS sheets.

Recently, researchers have developed the steel grid shear wall (SGSW) as a novel form of shear walls to overcome the limitations of traditional steel shear walls. In an SGSW, the conventional thin plate is substituted with a lattice of discrete steel members that directly transmit tension and compression in a grid configuration [55]. This design effectively mitigates the conventional issues associated with steel plate shear walls (SPSWs), particularly the sudden tension-field “snap” that occurs when the plate buckles; the grid members do not require reformation under load reversal, thus ensuring that the wall remains stable and free from noise even during load reversals. The grid members, composed of standard rolled sections rather than wide thin plates, are lighter and more straightforward to fabricate and erect [55]. Preliminary studies have demonstrated that SGSWs exhibit greater post-yield stiffness and energy dissipation—following the initial inelastic cycle—compared to comparable plain SPSWs, and do so at a reduced material cost. In summary, the SGSW effectively addresses numerous limitations inherent in SPSWs, including enhanced buckling resistance, improved access for services, and better constructability, while maintaining or enhancing seismic performance [56,57]. Chen et al. [57] proposed a type of steel grid shear wall as an innovative lateral load-bearing system. They subjected three specimens of steel grid shear walls with ten grid members to cyclic loading at a scale of 1:2. Additionally, a comparison was made between the performance of the steel grid shear wall and the traditional steel shear wall. The results indicated that the steel grid shear wall system exhibits excellent stiffness, ductility, and load-bearing capacity. Yu et al. [58]. evaluated the mechanical performance of self-restrained shear walls reinforced with CFRP (Carbon Fiber Reinforced Polymer) strips. They subjected two specimens, one with and one without diagonal CFRP-steel composite strips, to cyclic loading. According to the results obtained, the presence of the composite strips led to an increase in bearing capacity, ultimate bearing capacity, stiffness, and energy dissipation capacity. Furthermore, they determined the optimal arrangement of inclined composite strips through finite element analysis.As a result, the post-buckling behavior of steel shear walls and the concepts presented in the strip model were used to propose a novel lateral resisting system in this paper. This system is capable of addressing the limitations of traditional steel shear walls mentioned above.

This paper introduces a novel mesh steel shear wall (SGSW) as a lateral resisting system. Subsequently, a cyclic loading test was conducted on a SGSW specimen, and the hysteretic behavior of the SGSW was analyzed and discussed based on the experimental results. In the next stage, a finite element model of the SGSW was developed using ABAQUS software, and the modeling accuracy was validated by comparing the obtained results. Then, the mechanical performance of the SGSW and conventional steel plate shear wall (SPSW) was compared in terms of load-bearing capacity, energy dissipation capacity, initial stiffness, and ductility. Finally, based on the available results, the response modification coefficient of the SGSW was calculated and compared with an equivalent SPSW.

2. Steel Grid Shear Wall

Steel Grid Shear Wall (SGSW) is a new replacement for perforated steel plate shear wall. It consists of vertical and horizontal boundary elements (VBE and HBE) like common steel plate shear walls. However perforated web plate is replaced with a grid of steel bars. The section of the bar elements can be circle, Tee or angle. The bars are oriented in a suitable angle with boundary elements (Fig. 1). The bars are connected together at grid nodes. The end of the bars are connected to boundary elements through a welded or bolted connection to fish plates. This configuration of bars is consistent with strip model of web plate in steel plate shear walls. Under lateral loading of shear wall the bars act in tension or compression forces. In strip model of web plate the strips act only in tension because the compression strength of strips are negligible. However in SGSW the stiffness and strength of bars are more than strip plates and can be included in the structural behavior of shear wall.

One of the difficulty of steel plate shear wall with very thin web plate is workability and mounting of thin web plate and sometimes availability of very thin plates. However in SGSW the thin web plate can be replaced with a grid of bars with suitable bar size. So SGSW is a good SPSW for lowrise buildings and for top stories of tall buildings.

3. Design of SGSW specimen

In order to further investigate the mechanical behavior and failure mechanism of steel grid shear walls, an experimental study was conducted at structural laboratory of Ferdowsi University of Mashhad [59] on a single-story, single-bay specimen of a SGSW subjected to quasi-static loading. As proposed in this research, the steel grid shear wall is developed based on the concept of discretizing the steel plate shear wall using the strip model method. Initially, considering laboratory constraints such as space and the load capacity of the hydraulic jack, a SPSW model was designed in accordance with the AISC-341 standard [60]. In this regard, the steel plate was designed to have a shear capacity of 13 tons (ϕV_n). Here, V_n is the nominal shear strength of the panel, and φ is the strength reduction factor used in Load and Resistance Factor Design (LRFD), which accounts for uncertainties in material properties, fabrication, and construction tolerances.

$$V_n = 0.42 F_y t_w L_{cf} \sin 2\alpha \tag{1}$$

$$\phi = 0.9 \text{ (LRFD)}$$

where

F_y = specified minimum yield stress,MPa.

t_w= thickness of the steel plate, mm.

L_{cf}= clear distance between column flanges, mm.

The dimensions of the steel plate shear wall are shown in Fig. 1, with the steel frame dimensions measuring 1440 mm × 1130 mm and the steel plate thickness measuring 0.8 mm. Subsequently, the SGSW was constructed based on the SPSW design. The size and cross-section of the

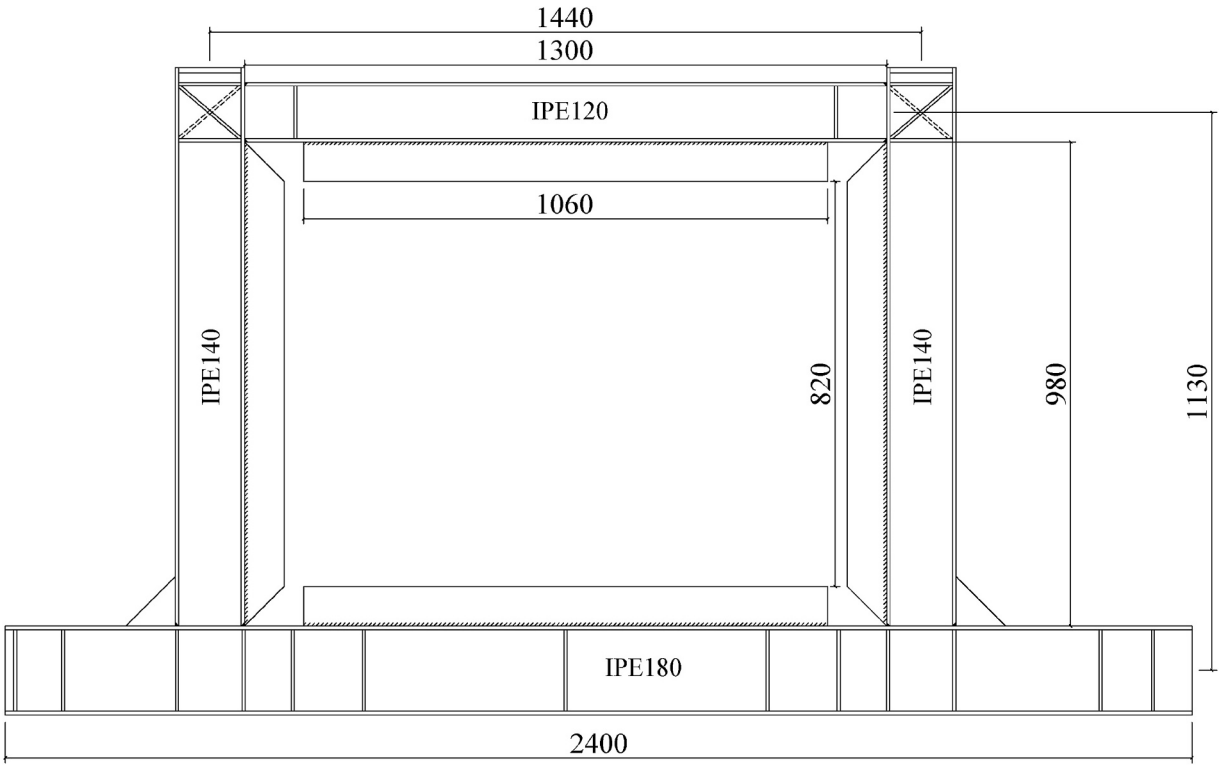

Fig. 1. Detail of SGSW.

frame members in both the SGSW and SPSW models were identical. Following this, the web plate in the SPSW was replaced with the grid of steel bars.

The angle of the steel bars in a SGSW can be calculated using Eq. (2), as proposed by Torbun et al. [8].

$$\tan^4\alpha = \frac{1+\frac{t_w L}{2A_c}}{1+t_w h\left[\frac{1}{A_b}+\frac{h^3}{360I_c L}\right]} \tag{2}$$

In this equation:

L = distance between the centerlines of vertical boundary elements (VBEs),

A_c= cross-sectional area of a column,

h = distance between the centerlines of horizontal boundary elements (HBEs),

A_b = cross-sectional area of a beam,

I_c = moment of inertia of a column,

The tension field angle was initially calculated to be 41° using eq. (2), based on the method proposed by Thorburn et al. [8], which considers the panel geometry, web thickness, and boundary element stiffness. Following this, a 40° diagonal angle was adopted in the experimental model, in accordance with the practical range suggested by AISC Design Guide 20 [61], which typically recommends values between 35° and 45°. Furthermore, the cross-sectional area of each steel bar was computed using eq. (3), also derived from the design approach stipulated in the same guide [61].

$$A_s = \frac{[L\cos(\alpha)+h\sin(\alpha)]t_w}{N} \tag{3}$$

In this equation, L represents the width of panel, h denotes the height of panel, t_w is the thickness of the web plate, and N is the number of steel grid elements (10 element in each direction). Assuming that each steel bar in the SGSW replaces a corresponding strip in the strip model of the SPSW, the required cross-sectional area for each member was calculated to be 65.03 mm^2. Accordingly, in the fabrication of the experimental specimen, twenty angle sections with dimensions of 20 × 1.8 mm and an actual cross-sectional area of 65.8 mm^2 were utilized.The exact orientation of the steel bars are presented in Fig. 2.

A model of a steel grid shear wall (SGSW) with angle members was designed for quasi-static testing. The specimen consists of three main sections: a steel frame, steel grid elements with an angle section, and fishplates. In the construction of the laboratory specimen, 10 angle diagonal members with a size of 20 mm were used in each direction. These members were welded to the fish plates at an angle of α = 40° relative to the vertical axis. To prevent premature out-of-plane deformation of the members, the intersection of steel grid members in two directions were connected to each other using filler plates and welding. The construction details of the SGSW specimen is shown in Fig. 3)a - c), and the exact dimensions of the specimen are presented in Table 1.

The beam-to-column connection is the moment-resisting and using fully welded fillet welds. Additionally, to prevent local buckling at the connection node, two diagonal and horizontal stiffeners along the beam flange have been employed. The details of the specimen construction are illustrated in Fig. 3 (a).

The fish-plates are designed to facilitate the connection of the steel grid members to the surrounding steel frame. The thickness of the fishplates was determined based on the maximum axial force expected in the diagonal grid members at the onset of failure, in accordance with the AISC 360–22 provisions [62]. The design ensured that the fishplates would remain elastic while safely transferring these forces to the boundary elements. In addition to the axial load demand, weld design considerations—such as the required weld length and throat size—were also taken into account. Based on these requirements, a 3 mm thick fishplate was selected to provide both structural adequacy and fabrication practicality. In this arrangement configuration, the grid members are attached to these plates using fillet welding, while the fish plates are connected to the surrounding frame through corner-to-corner welding to ensure alignment with the perimeter frame. The dimensions of these plates can be found in Fig. 3 (b).

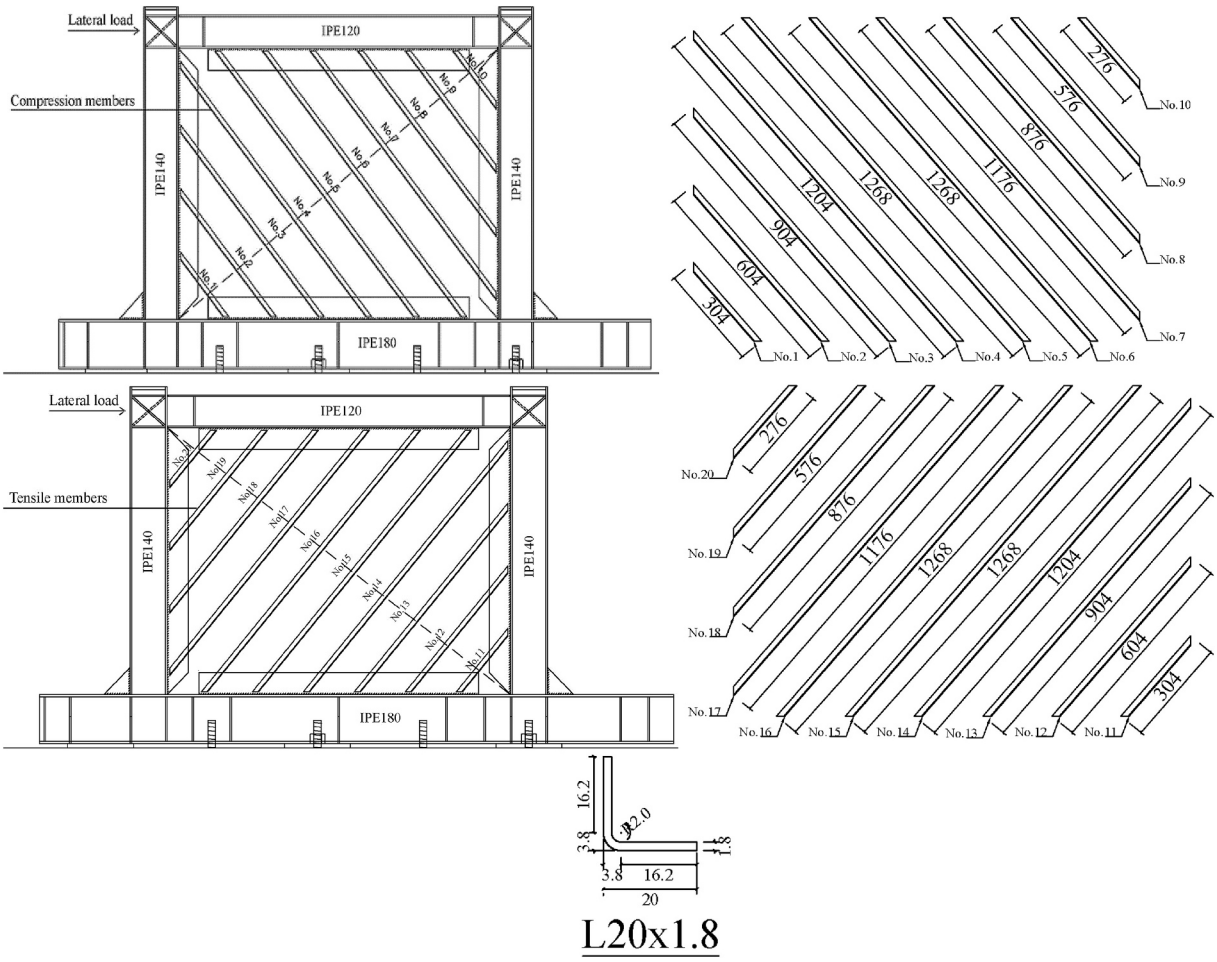

Fig. 2. Detail of steel grid members.

3.1. Mechanical properties of materials

In the fabrication of the steel grid shear wall specimen, ST37 [63] steel materials were utilized. In order to ascertain the mechanical properties of the individual components, tensile tests were executed following the guidelines stipulated by the ASTM E8M [64] standard. The specifications of the steel materials are summarized in Table 2.

3.2. Setup and program

The testing setup consists of seven components, including the solid laboratory floor, hydraulic jack, reaction frame, lateral bracing frame, load cell, data recording and processing device, and specimen-to-floor connecting elements, as illustrated in Fig. 4. For the application of cyclic lateral loading to the upper beam of the frame, a hydraulic jack is employed. The load is measured using a load cell that has a maximum capacity of ±300 kN. The hydraulic jack itself can achieve a maximum displacement of ±15 cm and has a maximum compressive and tensile capacity of ±800 kN. To prevent any out-of-plane deformation of the upper beam during loading, a lateral bracing frame has been implemented. This bracing frame serves the purpose of restraining both the rigid zone and the mid-span of the beam, as depicted in Fig. 4.

In the current study, the loading protocol was determined utilizing the displacement control method, consistent with the ATC24 [65] guidelines. As depicted in Fig. 5, the controller criterion for displacement control is the net displacement change per floor. Subsequently, to estimate the yield drift, a finite element analysis was conducted using Abaqus software. The yield displacement Δ_y was determined from the pushover analysis results of the finite element model by idealizing the backbone curve into a bilinear representation, following the procedure outlined in FEMA 356 [66]. the loading cycles were adjusted as follows to achieve the target net displacement values (Δ):

1- For displacements less than $3\Delta_y$, each displacement is repeated for three cycles. ($\Delta_y/3$ ، $2\Delta_y/3$،Δ_y ،$2\Delta_y$ ، $3\Delta_y$)
2- Until the specimen fails at displacements greater than $3\Delta_y$, each displacement is repeated twice.

Moreover, the lateral displacement of the specimen has been meticulously documented using linear variable differential transformers (LVDTs) No. 1 and 2, with a measurement accuracy of 0.1 mm. The placement of the displacement sensors can be observed in Fig. 6.

4. Test results

4.1. Failure process

During the initial six cycles, the specimen demonstrated a linear behavior with a displacement of 3.7 mm Fig. 7(a) This resulted in an out-of-plane deflection of grid bars that returned to its initial state when the loading direction changed. However, in the seventh cycle, a displacement of 9 mm led to out-of-plane buckling in the middle angle members Fig. 7(b). In the tenth cycle, a lateral displacement of 18 mm resulted in local buckling in all angle members, causing the cross-sectional area of the angles to deviate from its initial state Fig. 7(c). Further repetition of this load level led some plastic hinges at the two ends of the beam and

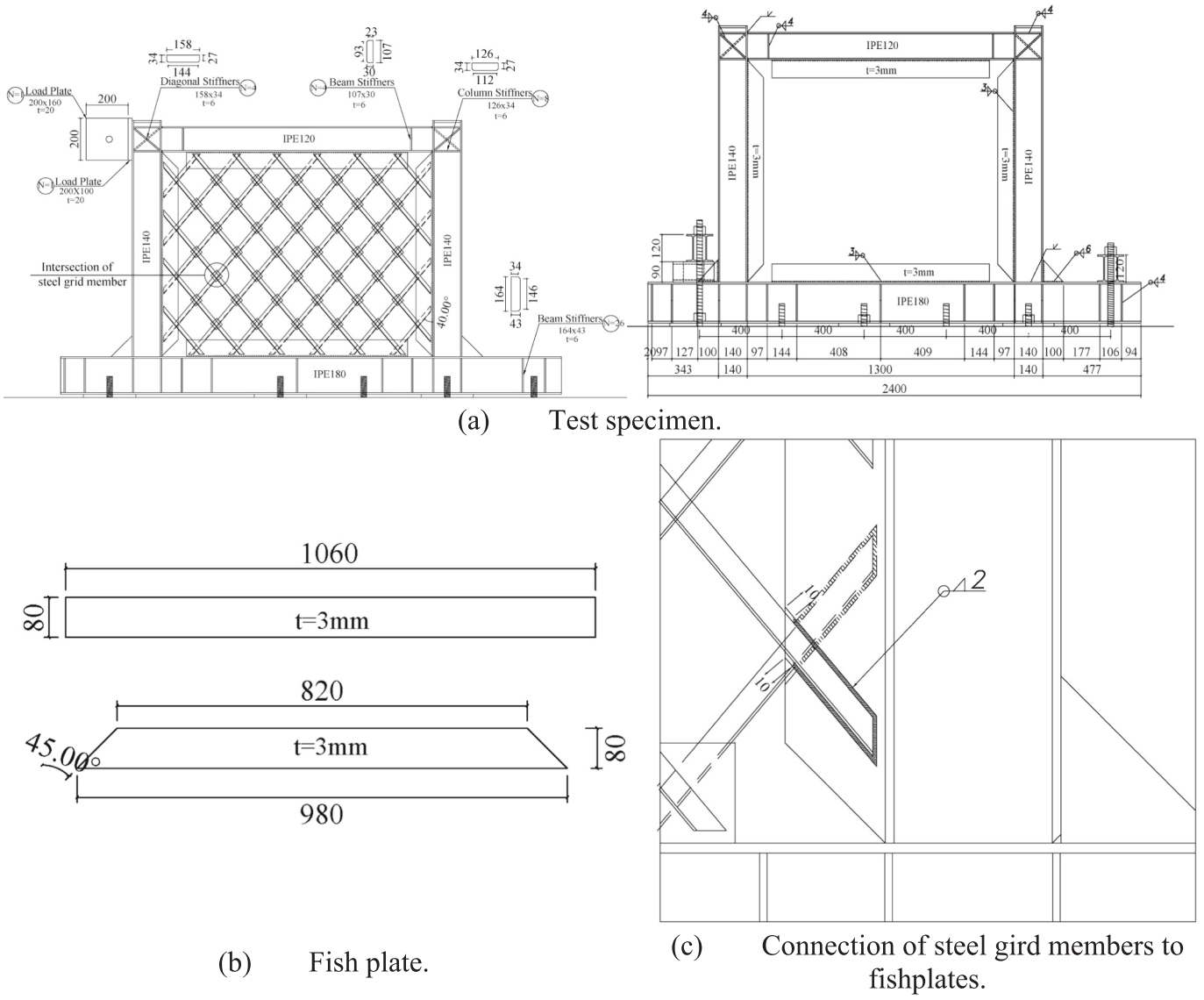

Fig. 3. Structural details of SGSW specimen.

Table 1
Details of SGSW specimen.

Specimen	Steel grid member section/ mm	Beam section/mm	Column section/mm	Fishplates/mm
SGSW	L20 × 1.8	IPE120(120 × 64 × 4.4 × 6.3)	IPE140(140 × 73 × 4.7 × 6.9)	3
SPSW	PL 0.8	IPE120(120 × 64 × 4.4 × 6.3)	IPE140(140 × 73 × 4.7 × 6.9)	3

Table 2
Steel material property.

Type	E (GPa)		Fy (MPa)		Fu (MPa)		Fy/fu		Elongation	
	Nominal	True	Nominal	True	Nominal	True	Nominal	True	Nominal	True
ST37-L20	179.44	180.13	341.43	342	415.40	515	0.82	0.66	0.241	0.216
ST37-IPE120	196.29	196.84	373.52	374	512.45	615.3	0.73	0.60	0.201	0.183
ST37-IPE140	191.11	191.35	353.68	354	497.87	605	0.71	0.58	0.215	0.195

the columns bases Fig. 7(d). In the sixteenth cycle, at a lateral displacement of 33 mm, angles 7, 16, and 17 ruptured Fig. 7(e). Finally, the loading process concluded in the eighteenth cycle due to the failure of the beam-to-column connection Fig. 7(f). The failure process of the SGSW specimen is depicted in Fig. 7.

4.2. Hysteresis curve

The cyclic loading curve of the SGSW specimen is presented in Fig. 8. In this experiment, the specimen underwent a total of 17 cycles, with the initial 3 cycles occurring in the linear region and the subsequent cycles

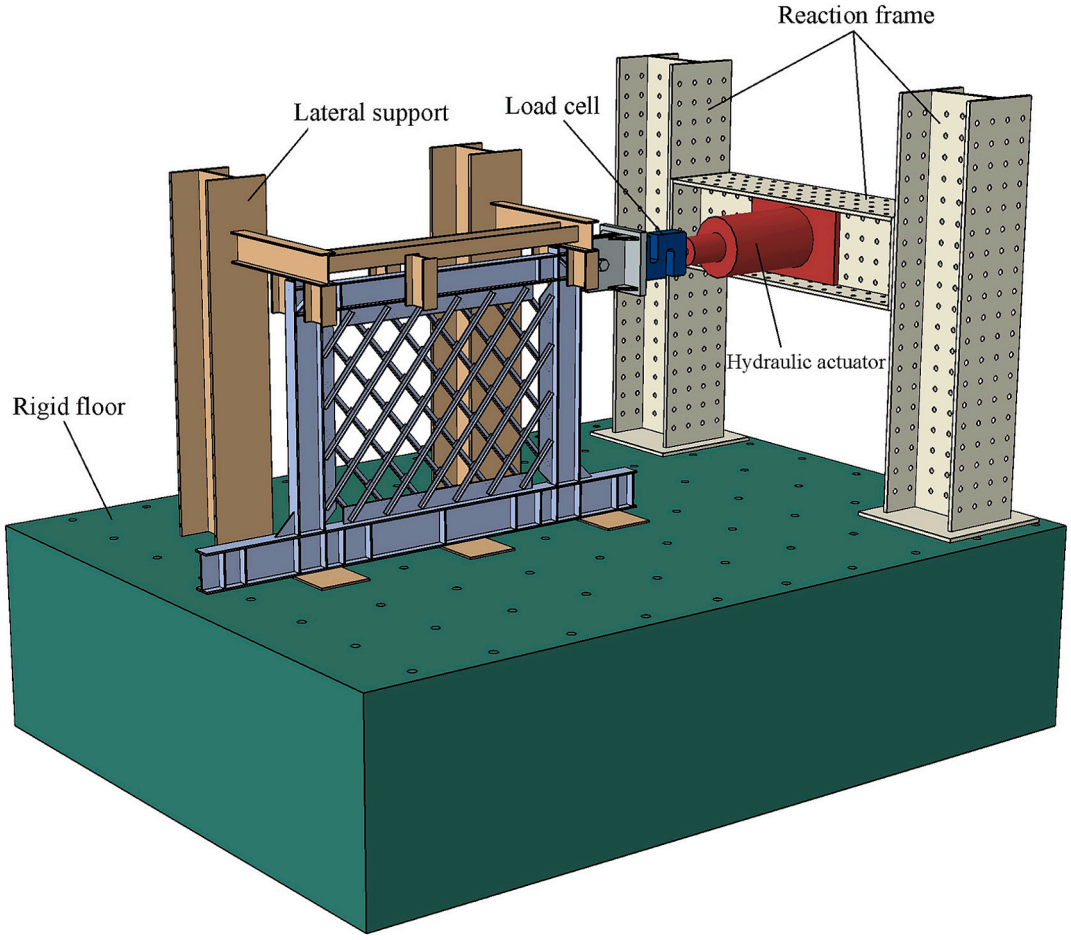

Fig 4. Test setup.

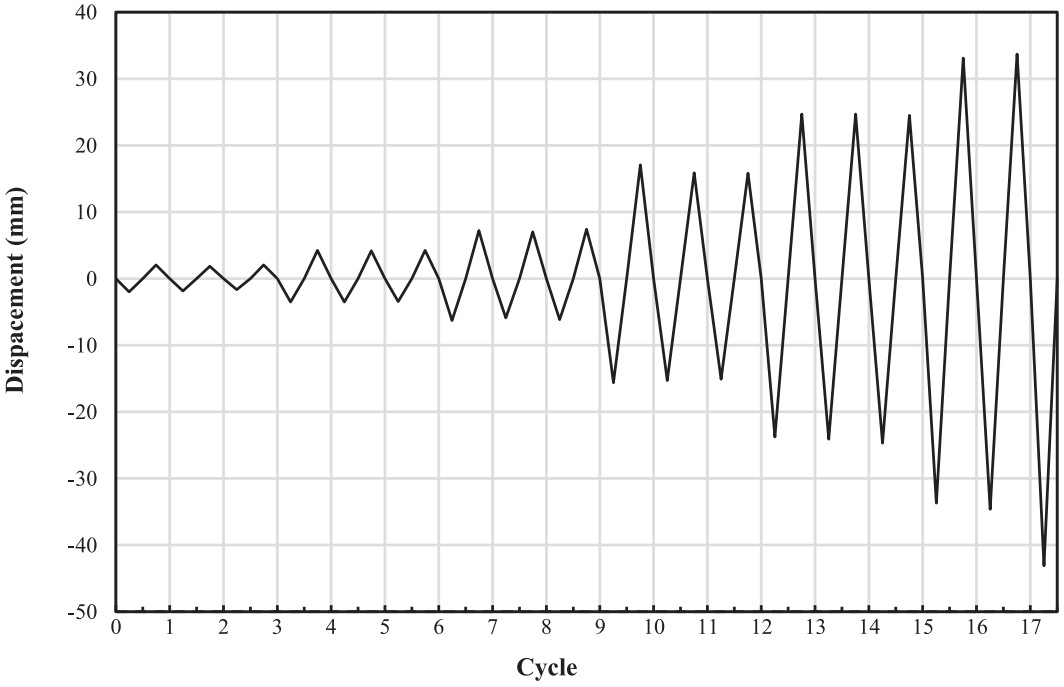

Fig. 5. Protocol loading.

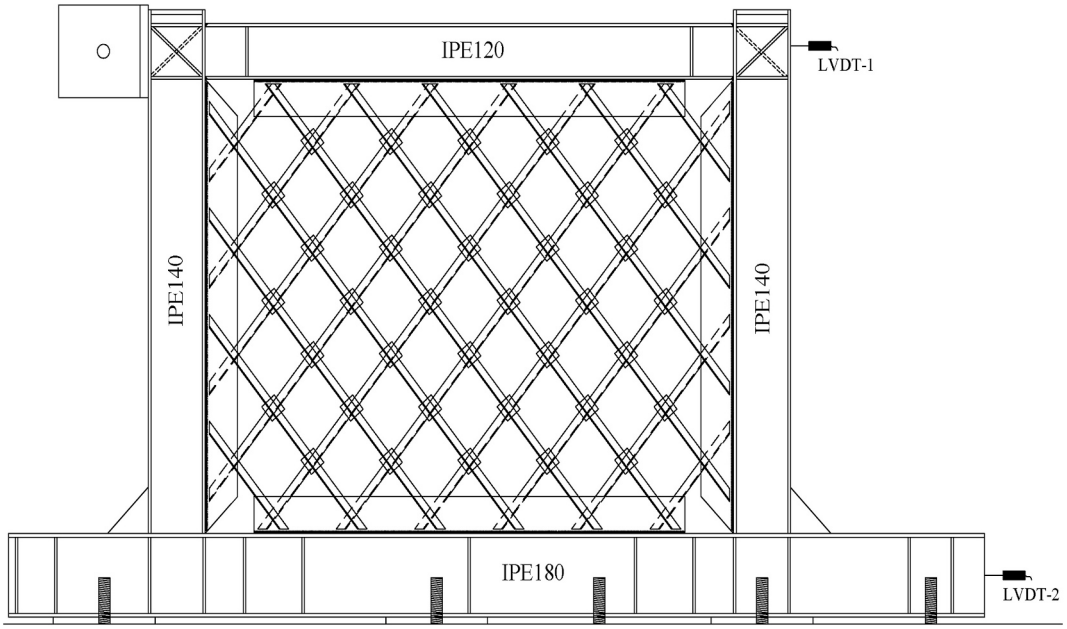

Fig. 6. Measuring point.

in the nonlinear region. During the sixteenth cycle, the first angle member ruptured, resulting in a decrease of the specimen's resistance by 11.8 % compared to the maximum shear resistance. Subsequently, in the seventeenth cycle, three more angle members ruptured, leading to a shear resistance reduction of 21.36 % relative to the maximum shear capacity.

Initially, the specimen exhibited similar stiffness in both the tensile and compressive regions. However, as the lateral displacement increased and plastic hinges formed in the grid elements, particularly in the mid-span elements of the frame, the hysteresis loop area expanded. At this stage, each cycle demonstrated a stable hysteresis curve with a considerable area. Ultimately, with the increase of displacement, all grid elements yielded, and plastic hinges formed at the beam and column ends. Moreover, buckling of the angles, resulted in a decrease in the load-bearing capacity of the system. As shown in Fig. 8, the maximum shear resistance of the specimen was 267.395 kN that occurred at a displacement of 16.2 mm, corresponding to a story drift ratio of approximately 1.43 %. It should be noted that the specimen was a single-story, single-bay frame with a clear height of 1130 mm. Although the results are presented in terms of absolute lateral displacement, the corresponding story drift ratios can be readily obtained. Specifically, the maximum displacements recorded in full load cycles (+33.63 mm and −34.5 mm) correspond to drift ratios of approximately +2.98 % and −3.05 %, respectively. These values fall within the drift ranges expected for structures designed for high-seismic performance.

4.3. Backbone curve

The backbone curve of SGSW is presented in Fig. 9. the maximum lateral displacement imposed on the specimen was 43.1 and 33.7 mm in the compressive and tensile region, respectively. The ductility values for the tensile and compressive regions were determined to be 8.14 and 8.98, respectively. Relevant information concerning the shear resistance, stiffness, and ductility of the SGSW can be found in Table 3.

4.4. Strength and stiffness degradation

To further investigate the changes in SGSW behavior during loading stages, the capacity degradation curve, stiffness reduction curve, and consumed energy ratio were utilized. The variations in the shear capacity of the SGSW can be observed in Table 4. Fig. 10 illustrates the shear capacity degradation of the SGSW. The Eq. (4) calculates the ratio of shear capacity degradation [67]:

$$\lambda = F_i / F_{i-1} \tag{4}$$

In this equation, F_i represents the maximum resistance in the i-th cycle, and F_{i-1} represents the maximum resistance in the (i-1)-th cycle of each loading level.

All capacity ratios observed during the first five loading levels exceed 0.9. However, in the final level, the ratio dropped slightly to 0.89 due to fracture of some grid elements, which marked the onset of system failure. Based on the results, the load-bearing capacity of the SGSW remains relatively stable and undergoes no significant changes across similar loading levels. Furthermore, the ratio of changes in load-bearing capacity initially increased in the first two loading levels and then exhibited a decreasing trend.

In order to investigate the pattern of damage formation and formation of plastic hinges in the specimen during loading, the stiffness degradation factor has been employed. The stiffness degradation for both tensile and compressive regions is presented in Table 5. Additionally, Fig. 11 illustrates the stiffness degradation curve during loading. The secant stiffness for each cycle is determined using Eq. (5):

$$K_i = \frac{F_{pull} - F_{push}}{X_{pull} - X_{push}} \tag{5}$$

In this equation, F represents the ultimate resistance in each direction, and X corresponds to the displacement associated with these forces.

Based on the obtained results, Initially, prior to yielding, the system exhibits predominantly elastic behavior, and stiffness remains relatively stable due to the intact geometry and full section effectiveness of the angle members. As cyclic loading progresses, local yielding commences in the diagonal members, particularly in mid-length regions subjected to maximum bending and axial forces. With continued loading, local buckling initiates in several members, resulting in a reduction of their effective stiffness. Concurrently, the repeated stress reversals induce cyclic degradation in material stiffness [68,69] (i.e., Bauschinger effect and local plasticity), leading to a gradual loss of secant stiffness. The congruence in degradation trends between the tensile and compressive regions is indicative of the symmetric arrangement and behavior of the diagonal grid members, as well as the nearly balanced energy

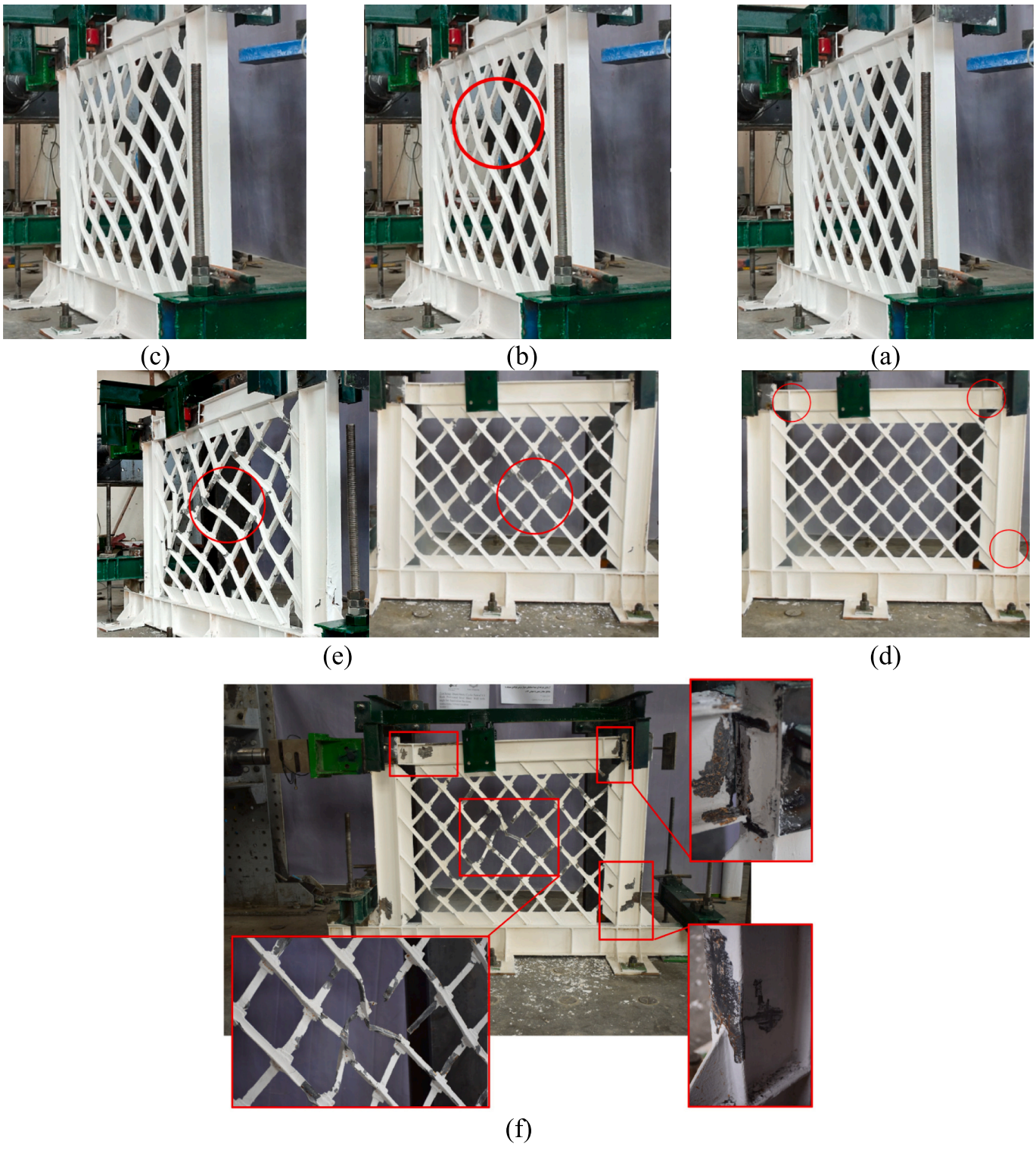

Fig. 7. The failure process of the SGSW specimen.

dissipation under forward and reverse cyclic displacements.

4.5. Energy dissipation performance

The area of each cycle of the hysteresis curve and the energy dissipation coefficient (Ed) of the SGSW specimen are presented in Table 6. The energy dissipation coefficient [70] can be calculated from eq. (6):

$$E_d = \frac{S_{(ABC+CDA)}}{S_{(OBE+ODF)}} \tag{6}$$

Based on Fig. 12, $S_{(ABC+CDA)}$ represents the area enclosed by the hysteresis curve in each cycle, while $S_{(OBE+ODF)}$represents the area enclosed by the triangle formed between the point of force reversal and the horizontal axis of coordinates.

According to Table 6, the maximum energy dissipation coefficient

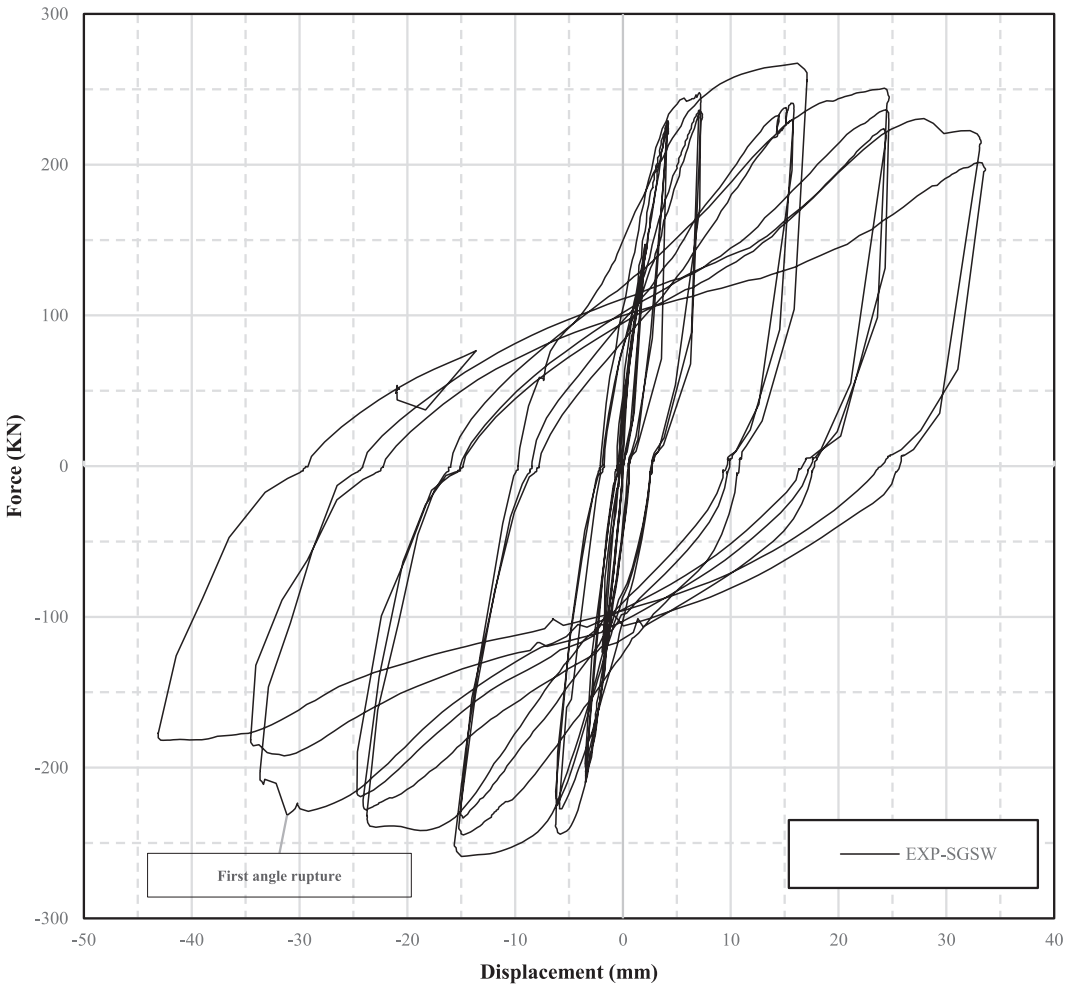

Fig. 8. The hysteresis curve of SGSW.

(Ed) in this system is 1.91, which exceeds that of a SPSW [71] (with an energy dissipation coefficient of approximately 1.2). Additionally, Fig. 13 (a) and (b) illustrate the energy dissipated in each cycle and the cumulative energy dissipation, respectively. Notably, the SGSW specimen exhibits a maximum area of one cycle amounting to 13.54 kN.m. (See Fig. 13 (a).)

5. Numerical modeling

For more investigating the behavior of SGSW a numerical model was simulated using the finite element software ABAQUS [72]. Subsequently, the accuracy of the finite element model was verified through comparison with experimental results. Due to practical constraints and the substantial expenses associated with laboratory testing, a comparative analysis of the mechanical performance of the steel grid shear wall (SGSW) and the steel plate shear wall (SPSW) was carried out based on results obtained from finite element analysis.

5.1. Model description

The finite element model of the SGSW system included beams, columns, fishplates, and grid members with angle cross-sections. To capture the complex interaction of components under cyclic loading, the model accounted for axial, flexural, torsional, and shear behavior of all members. Accordingly, all parts were modeled using S4R shell elements, which are 4-node, reduced-integration, finite-strain elements suitable for thin-walled steel components and effective in simulating both local and global deformations. After assembling all components of the SGSW system, the model parts were merged into a single unified geometry to ensure continuity of the mesh and to avoid numerical inconsistencies at element interfaces. This merging process was performed prior to applying loading and boundary conditions and was critical for accurately capturing the global response of the structure during simulation. The boundary conditions and loading protocol mirrored the experimental setup, ensuring consistency between numerical and physical simulations. Displacement-controlled lateral cyclic loading was applied to the upper beam, replicating the ATC-24 protocol followed during the test. The material properties assigned to the steel components were based on the experimentally obtained tensile test results reported in Table 2. As the cyclic behavior of structural steel under low-cycle loading differs significantly from monotonic conditions—due to effects such as the Bauschinger effect and cyclic hardening—traditional monotonic-based models may lead to inaccurate predictions. To address this, a combined isotropic–kinematic hardening model, based on the Chaboche formulation [68,69], was implemented in ABAQUS through the Combined Hardening option [72]. This model enables the accurate representation of cyclic plasticity phenomena, including strain accumulation, cyclic stiffness degradation, and reversal effects. To realistically simulate geometric imperfections, which play a significant role in triggering local and global buckling under cyclic loads, a two-step analysis procedure was adopted. First, an eigenvalue buckling analysis was conducted to extract the first three mode shapes of the system. These modes were then scaled and superimposed to generate an imperfection field. For the SPSW, following Eurocode 3 (EN 1993-1-5)

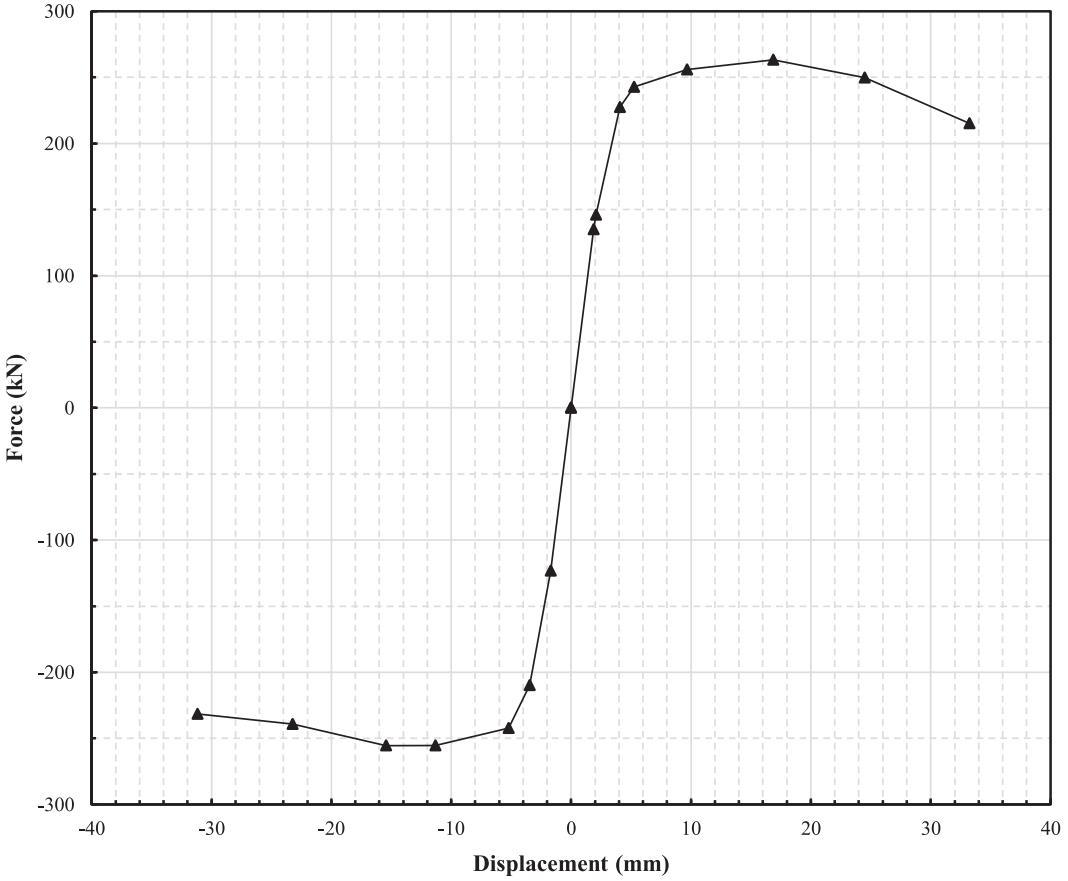

Fig. 9. The backbone curve of SGSW.

Table 3
Backbone curve specifications.

Specimen		Yield point		Peak point		Ultimate point		Ductility coefficient
		Load (kN)	Displacement (mm)	Load (kN)	Displacement (mm)	Load (kN)	Displacement (mm)	
SGSW	Pull	227.55	4.08	263.24	16.86	215.31	33.22	8.14
	Push	209.77	3.47	255.52	15.43	231.63	31.16	8.98
	Mean	218.66	3.77	259.38	16.145	223.46	32.19	8.54

Table 4
The shear capacity degradation of SGSW.

Load level	Number of cycles	Cumulative number of cycles		SGSW					
			Pull	Push	Mean		Pull	Push	Mean
			F_i(kN)	F_i(kN)	$\overline{F_i}$(kN)		$\lambda = F_i/F_{i-1}$	$\lambda = F_i/F_{i-1}$	$\overline{\lambda} = \overline{F}_i/\overline{F}_{i-1}$
	1	1	143.99	123.19	133.59				
$\Delta_y/3$	2	2	135.23	123.45	129.34	cycle2/cycle1	0.94	1.00	0.97
	3	3	147.19	112.19	129.69	cycle3/ cycle2	1.09	0.91	1.00
	1	4	226.94	199.82	213.38				
$2\Delta_y/3$	2	5	222.62	209.85	216.23	cycle2/cycle1	0.98	1.05	1.01
	3	6	227.91	205.67	216.79	cycle3/ cycle2	1.02	0.98	1.00
	1	7	246.43	239.05	242.74				
Δ_y	2	8	235.10	227.35	231.22	cycle2/cycle1	0.95	0.95	0.95
	3	9	231.35	223.50	227.43	cycle3/ cycle2	0.98	0.98	0.98
	1	10	256.15	255.61	255.88				
$2\Delta_y$	2	11	238.35	244.71	241.53	cycle2/cycle1	0.93	0.96	0.94
	3	12	227.28	231.27	229.27	cycle3/ cycle2	0.95	0.95	0.95
	1	13	245.13	238.88	242.00				
$3\Delta_y$	2	14	234.51	228.20	231.35	cycle2/cycle1	0.96	0.96	0.96
	3	15	221.19	219.40	220.29	cycle3/ cycle2	0.94	0.96	0.95
$4\Delta_y$	1	16	214.08	211.24	212.66				
	2	17	197.52	185.61	191.57	cycle2/cycle1	0.92	0.87	0.89

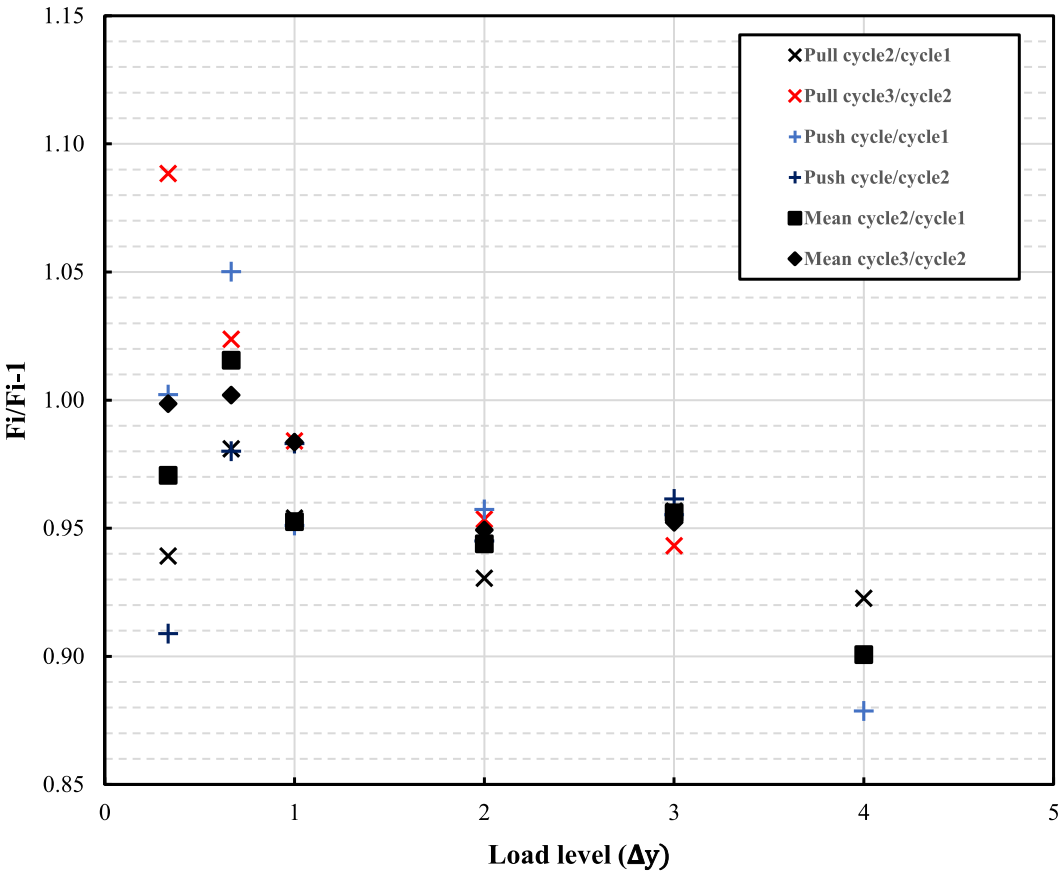

Fig. 10. Shear capacity degradation of SGSW.

Table 5
The secant stiffness degradation.

Load level	Number of cycles	Cumulative number of cycles	SGSW					
			Pull	Push	Full loop	Pull	Push	Full loop
			K_i	K_i	K_i	K_i/K_0	K_i/K_0	K_i/K_0
	1	1	69.94	63.38	66.75	1	1	1
$\Delta_y/3$	2	2	71.81	65.68	68.75	1.03	1.04	1.03
	3	3	71.66	69.06	70.51	1.02	1.09	1.06
	1	4	54.68	57.70	56.06	0.78	0.91	0.84
$2\Delta_y/3$	2	5	52.93	60.51	56.36	0.76	0.95	0.84
	3	6	53.93	59.41	56.40	0.77	0.94	0.84
	1	7	34.18	38.17	36.03	0.49	0.60	0.54
Δ_y	2	8	32.75	38.69	35.42	0.47	0.61	0.53
	3	9	31.38	36.55	33.72	0.45	0.58	0.51
	1	10	15.00	16.57	15.74	0.21	0.26	0.24
$2\Delta_y$	2	11	15.02	16.53	15.75	0.21	0.26	0.24
	3	12	14.40	15.36	14.87	0.21	0.24	0.22
	1	13	9.92	10.18	10.05	0.14	0.16	0.15
$3\Delta_y$	2	14	9.52	9.59	9.55	0.14	0.15	0.14
	3	15	9.08	9.01	9.05	0.13	0.14	0.14
$4\Delta_y$	1	16	6.45	6.34	6.39	0.09	0.10	0.10
	2	17	5.88	5.41	5.64	0.08	0.09	0.08

recommendations [73], an imperfection scale factor of min(a/200, b/200), approximately 0.005 for a panel height of 0.98 m, was applied to the first three buckling modes. Subsequently, for the SGSW, an imperfection scale factor of L/250, approximately 0.005 for diagonal bars of 1.268 m, was used to account for local imperfections in the grid members, consistent with Eurocode 3 (EN 1993-1-1) [74]. These values ensured numerical stability and accurate representation of the hysteretic response. This initial imperfection configuration was introduced into the nonlinear cyclic loading analysis. With the finite element model fully defined in terms of geometry, material behavior, boundary conditions, and initial imperfections, the next step was to ensure numerical stability and accuracy. Therefore, a convergence study was carried out to determine an appropriate mesh density, followed by verification of the numerical model through comparison with the experimental results, as detailed in the subsequent sections.

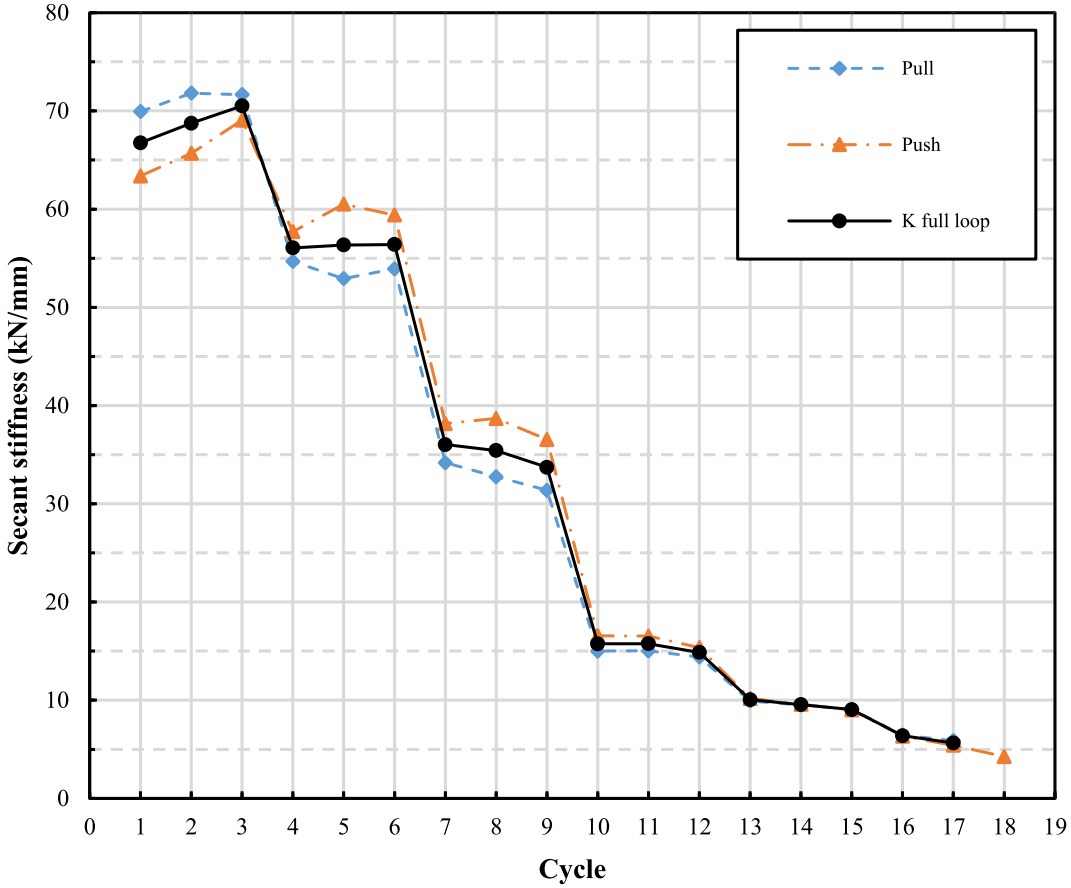

Fig. 11. The stiffness of SGSW specimen.

Table 6
The energy dissipation coefficient.

Load level	Number of cycles	Cumulative number of cycles	SGSW	
			S	E_d
	1	1	0.12	0.45
$\Delta_y/3$	2	2	0.12	0.50
	3	3	0.11	0.44
	1	4	0.65	0.79
$2\Delta_y/3$	2	5	0.49	0.58
	3	6	0.48	0.57
	1	7	2.18	1.33
Δ_y	2	8	1.73	1.15
	3	9	1.75	1.14
	1	10	7.96	1.91
$2\Delta_y$	2	11	5.79	1.56
	3	12	4.85	1.37
	1	13	10.65	1.83
$3\Delta_y$	2	14	9.14	1.63
	3	15	8.13	1.52
	1	16	13.54	1.91
$4\Delta_y$	2	17	11.40	1.75
$5\Delta_y$*	1	18	6.58	1.43

S: represents the area enclosed by the hysteresis loop in each loading cycle, measured in kN·m, which indicates the energy dissipated by the specimen during that cycle.

* The final loading cycle corresponding to $5\Delta_y$ was not fully completed.

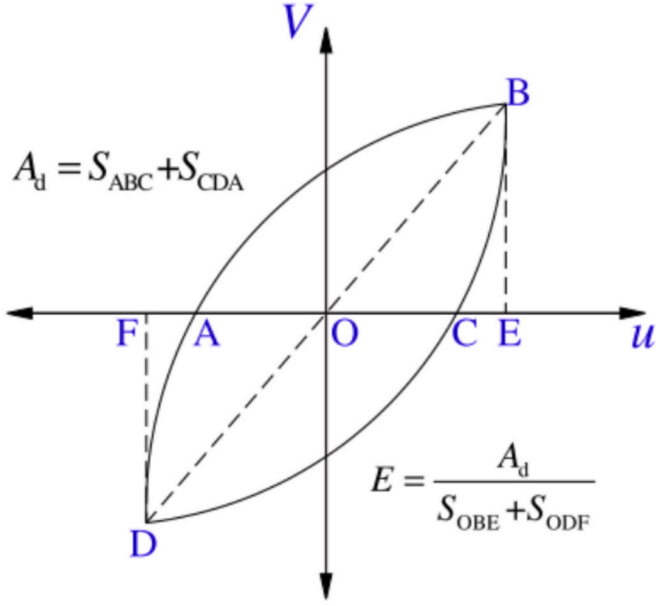

Fig. 12. Ed calculation [70].

5.2. Convergence of finite element analysis

Due to the presence of multiple buckling modes in the SGSW model, numerical convergence is not achieved with a large mesh size. Consequently, various mesh densities were investigated, and ultimately, convergence in responses was achieved at a mesh size of 20 mm. Fig. 14 illustrates the sensitivity analysis results of mesh density based on the maximum specimen resistance under incremental loading analysis.

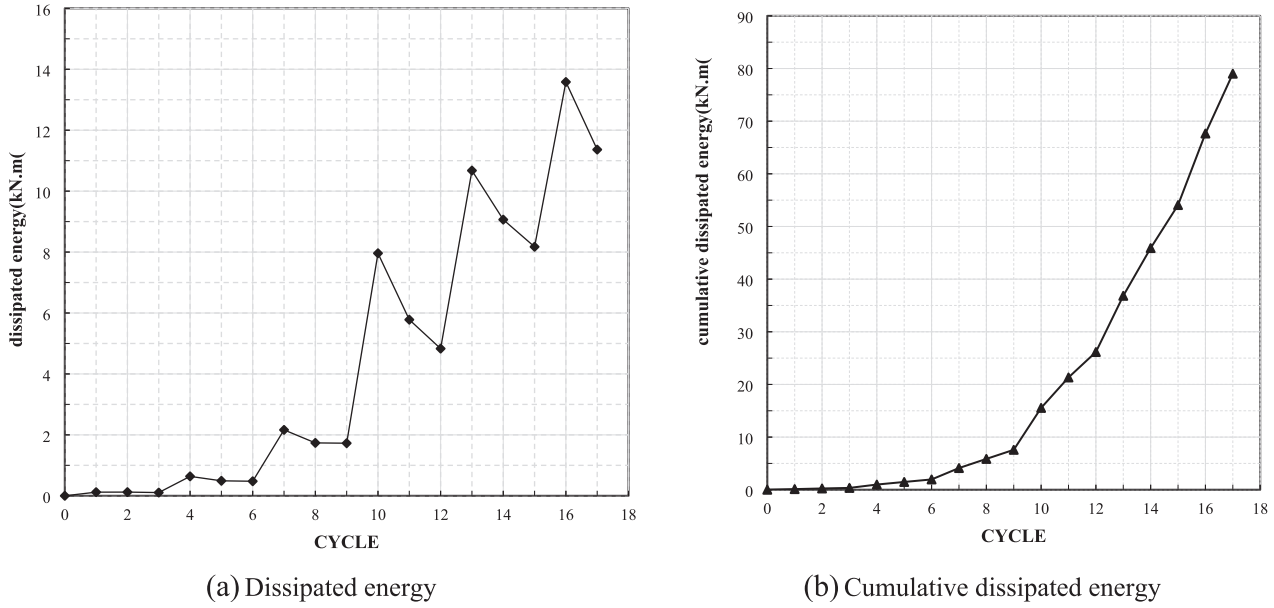

(a) Dissipated energy (b) Cumulative dissipated energy

Fig. 13. The dissipated energy of SGSW specimen.

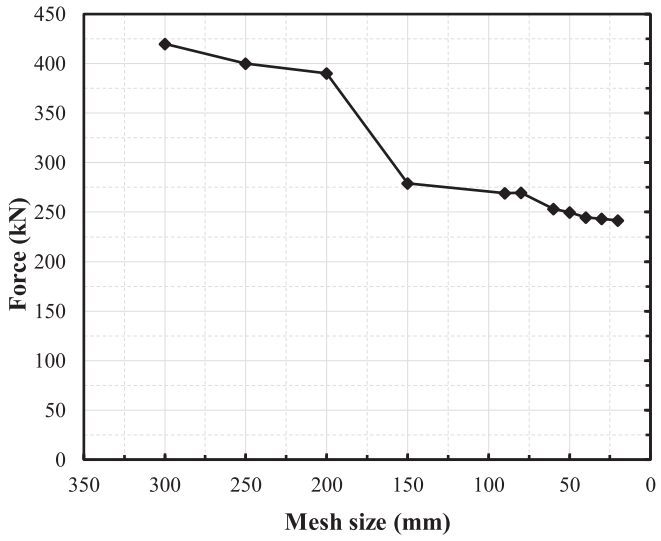

Fig. 14. The convergence of finite element analysis.

5.3. Verification of FEM Model

In order to validate the finite element model, a comparison was made between the hysteresis curve (Fig. 15(a)), backbone curve (Fig. 15 (b)), and cumulative dissipated energy (Fig. 15 (c)) with the corresponding experimental results.

As shown in Fig. 15 (a) and 15(c), while the general agreement between the experimental and numerical models is strong, a slightly higher cumulative energy dissipation is observed in the experimental specimen. This can be attributed to local mechanisms present in the physical test—such as friction at connections, slight slack or looseness, micro-yielding near welds, and minor out-of-plane deformations—that are not explicitly modeled in the FE simulation. Additionally, the combined hardening material model [72] used in the FEM, while capable of simulating global cyclic behavior, does not capture localized damage or progressive softening effects following rupture initiation. Despite these limitations, the relative difference in cumulative energy dissipation remains within an acceptable margin, validating the numerical model's reliability for simulating the global seismic behavior of the SGSW system.

The findings revealed a strong correlation between the failure mode, initial stiffness, and ultimate strength of experimental results and the analytical model. The maximum shear strength, initial stiffness, and cumulative dissipated energy values for both the finite element model and the experimental model are presented in Table 7.

Furthermore, Fig. 16 illustrates a side-by-side comparison of the deformed shapes and stress distributions between the experimental specimen and the finite element model. The FEM results accurately replicate the global displacement pattern and lateral deformation observed in the test. Notably, the formation of plastic hinges at the beam-column connections and at mid-span regions of diagonal grid elements is consistent in both cases. The stress concentration zones in the FEM—particularly at the ends of upper beam and lower column bases—correspond closely with the regions of local yielding and observed damage in the physical test. This level of agreement validates the modeling approach and supports the use of the FEM in subsequent parametric and comparative analyses presented in the following sections.

5.4. Yielding conditions of boundary elements

To investigate the structural response of the SGSW under cyclic loading, the yielding behavior of the boundary elements and fish plates was evaluated through finite element analysis, the yielding behavior of vertical boundary elements (VBEs), horizontal boundary elements (HBEs), and fish plates was analyzed through finite element method (FEM) to elucidate the response of the SGSW under quasi-static cyclic loading. The FEM results indicated that the maximum von Mises stresses developed in the boundary elements were as follows: 463.0 MPa in the VBEs, 486.3 MPa in the upper HBE, and 374.1 MPa in the lower HBE. Additionally, the maximum von Mises stress in the fish plates was observed at the small end regions of these plates, reaching 372.7 MPa, slightly exceeding the yield stress of 342 MPa reported in Table 2. The yielding process of the surrounding elements occurred in the following sequence: the web elements yielded first, followed by the upper beam in the 7th cycle, and the side columns in the 10th cycle, while the lower beam did not enter the yielding zone. Furthermore, localized yielding in the fish plates occurred in the 7th cycle, with a maximum von Mises stress of 372.7 MPa near the welded connections (Fig. 16). This yielding

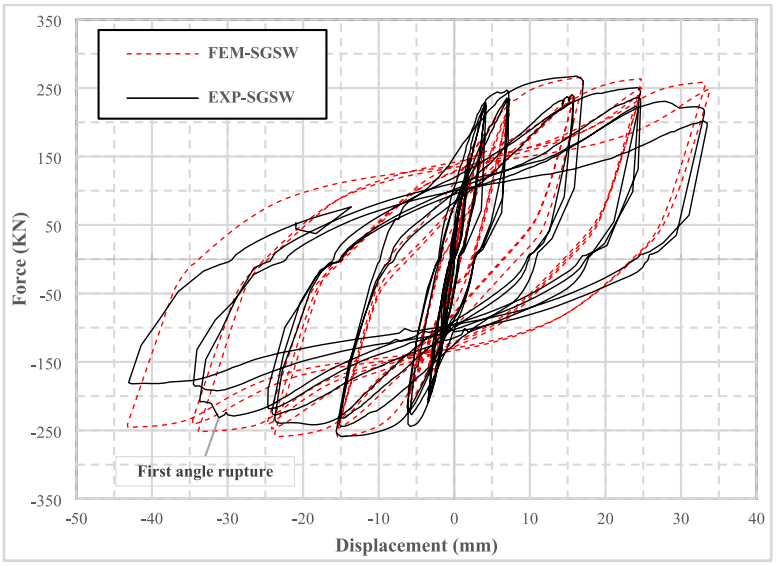

(a) The comparision of hysteresis curve.

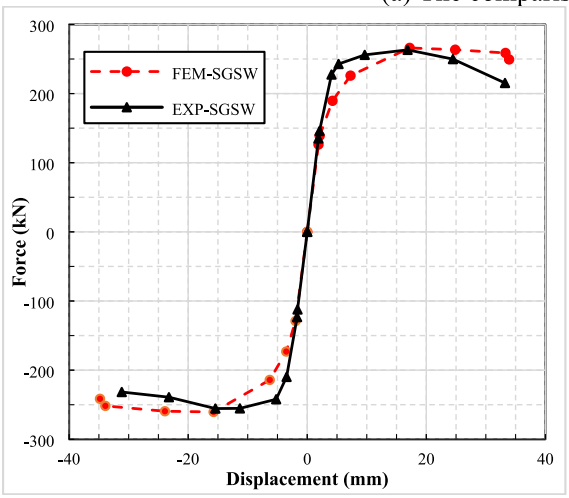

(b) The comparision of backbone curve.

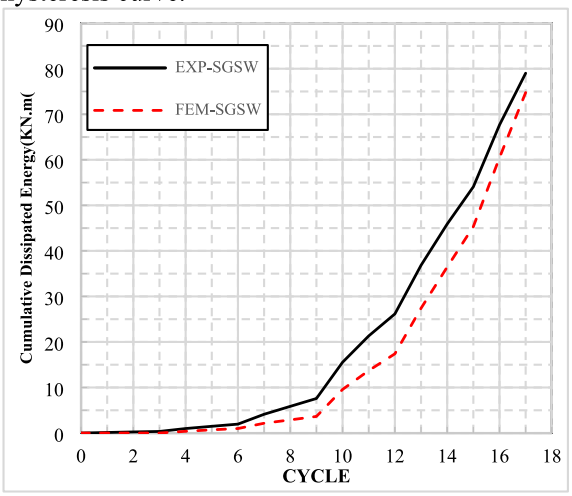

(c) The comparision of Cumulative Dissipated Energy.

Fig. 15. The comparision between FEM and experimental results.

Table 7
The comparision of FEM and experimental results.

Specimen	SGSW								
	Cumulative dissipated energy (kN m)			K0 (kN/mm)			Peak load (kN)		
	Test	FEM	Test/FEM	Test	FEM	Test/FEM	Test	FEM	Test/FEM
Pull	267.30	266.06	1.005	69.94	66.71	1.048			
Push	258.95	260.47	0.994	63.38	65.72	0.964	79.08	74.76	1.058
Mean	263.12	263.26	0.999	66.66	66.21	1.007			

was confined to small regions and did not significantly affect the overall response, as evidenced by the stable hysteresis curves (Fig. 17). Fig. 16 illustrates the deformation patterns and locations of plastic hinges, demonstrating strong agreement between experimental and numerical results.

6. Results and discussion

6.1. Comparison between SGSW and SPSW

In order to conduct a comprehensive comparison between the behaviors exhibited by SGSW and SPSW, hysteresis curves obtained from experimental SGSW specimens, as well as finite element models of both SGSW and SPSW, were extracted and evaluated. As a result, Fig. 17 shows the hysteresis curve, backbone curve, and cumulative dissipated energy for each of the aforementioned models. The cumulative energy

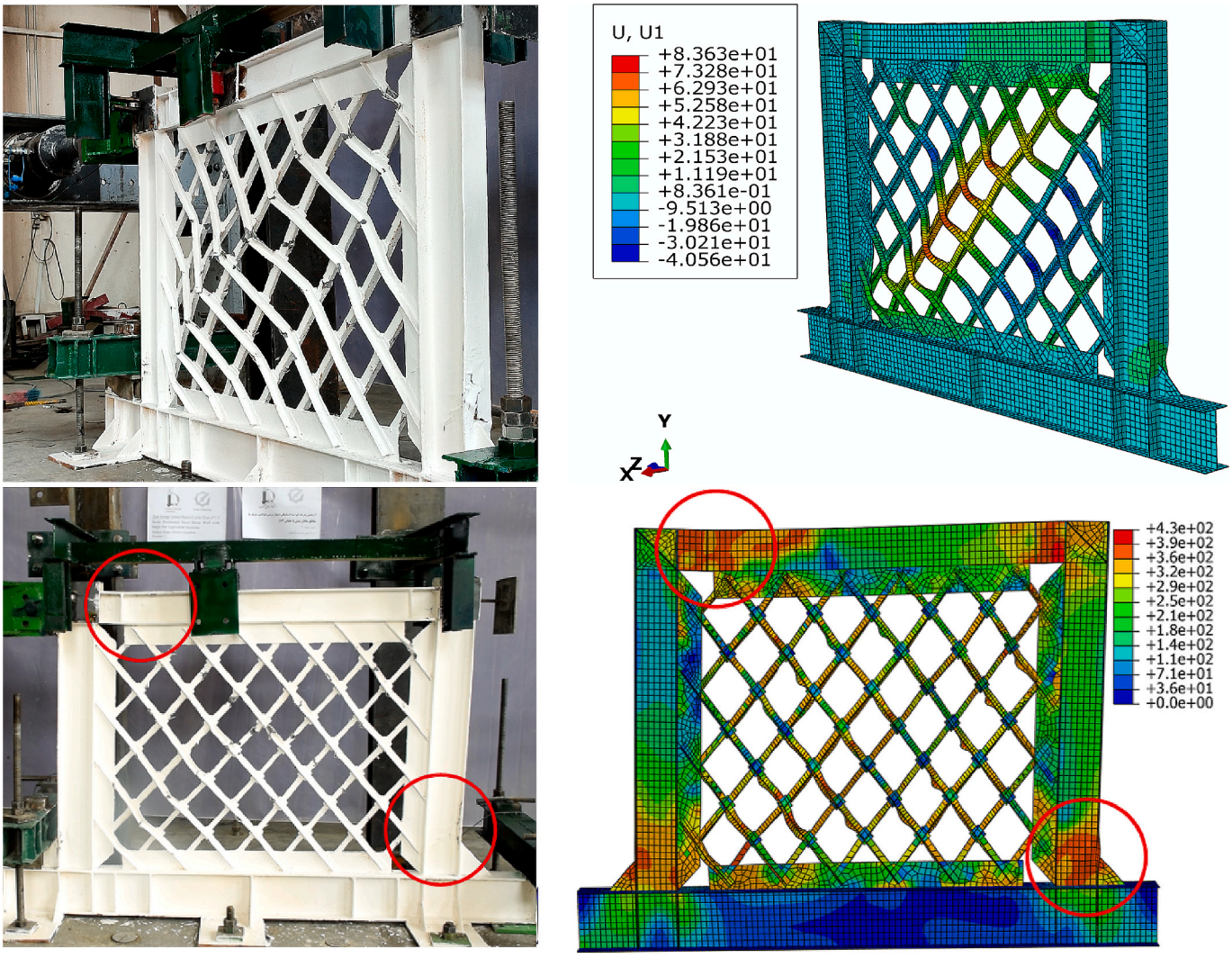

Fig. 16. The comparision of displacement between FEM and experimental results.

dissipation for the experimental specimen, FEM-SGSW, and FEM-SPSW models was consistently calculated by integrating the enclosed area within each hysteresis loop for all loading cycles. For the experimental data, a custom Python script was used to numerically integrate the measured load–displacement curves cycle by cycle. Similarly, for the FEM models, the hysteresis curves were extracted from the numerical outputs and the cumulative dissipated energy was recalculated using the same area-based method to ensure consistency across all comparisons. Additionally, a summarized overview of the results can be found in Table 8.

As observed, the initial stiffness of SGSW and FEM-SGSW is approximately 18.4 % higher than that of FEM-SPSW. Additionally, the maximum shear resistance of SGSW is roughly 17.95 % less than that of FEM-SPSW. Furthermore, As observed from Table 8, the cumulative dissipated energy of the FEM-SPSW model is very close to that of the experimental SGSW specimen at approximately 3 % story drift.

Fig. 18 shows the comparison of dissipated energy in different cycles during the analysis between SGSW and SPSW systems. As observed, EXP-SGSW exhibits a higher energy dissipation in the first 12 cycles. Eventually, SPSW energy dissipation surpasses that of SGSW after the 13th cycle where most the steel grid members have yielded but some zones in the steel plate were still in the elastic phase which caused the increase in the dissipated energy of the SPSW on the next cycles due to the yielding of those zones.Table 9 shows the details of energy dissipation in each cycle of the mentioned models.

6.2. Response modification factor

Due to the complexity and time-intensive aspect of nonlinear structural analysis, scholars have consistently persued a straightforward approach to incorporate the energy dissipation effects arising from the nonlinear deformation of structures in their computations. Consequently, the Response modification factor, denoted as R, within the framework of the National Earthquake Hazards Reduction Program (NEHRP 1988) [75], serves as a coefficient for modifying the linear elastic response. In this study, the equations provided by Uang [76] were employed to determine R factor. as illustrated in Eq. (7):

$$R = R_{\mu}\Omega \tag{7}$$

R_{μ} is the ductility reduction factor, which allows the elastic design force to be reduced to the current yield strength level due to the cyclic energy dissipation capacity of the structure and Ω represents the system overstrength factor. Structural overstrength refers to the phenomenon in which structures exhibit resistance higher than their intended design values. This can be attributed to several factors, such as internal mechanisms redistributing forces, underestimation of material strength, strain hardening effects, limitations on system behavior deflections, and tolerances in member sizes [77]. Fig. 19 presents General structural response curve.

According to the method proposed by Uang [76], the overstrength

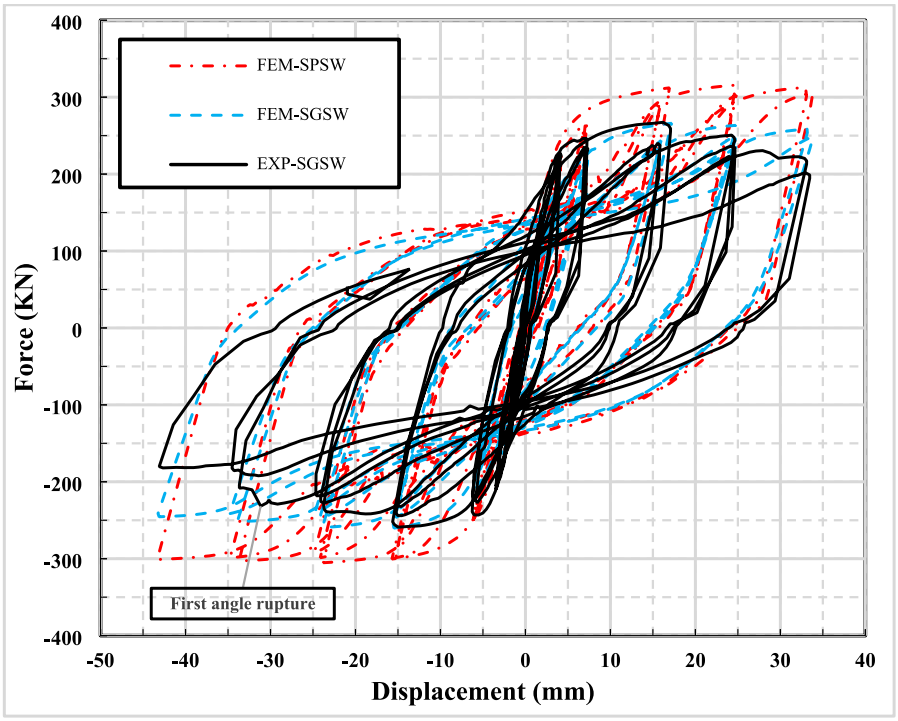

(a) The comparison of the hysteresis curve.

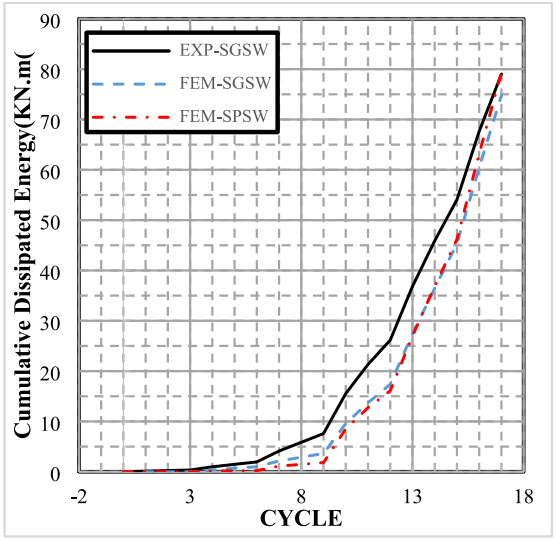

(c) The comparison of the Cumulative Dissipated Energy

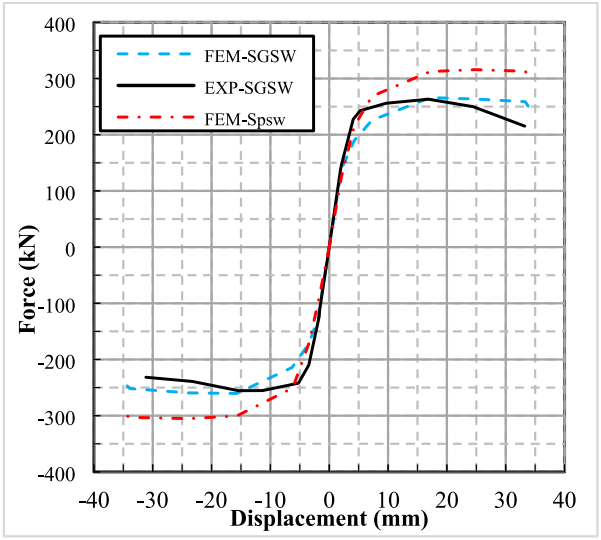

(b) The comparison of the backbone curve.

Fig. 17. The comparison between SGSW and SPSW.

Table 8
The comparision between SGSW and SPSW results.

Specimen	Peak load (kN)			K0 (kN/mm)			Cumulative dissipated energy
	Pull	Push	Mean	Pull	Push	Mean	(kN m)
SGSW	267.30	258.95	263.12	69.94	63.38	66.66	79.08
FEM-SGSW	266.06	260.47	263.26	66.71	65.72	66.21	74.76
FEM-SPSW	315.79	305.26	310.53	60.47	52.09	56.28	79.41

coefficient Ω and the ductility reduction factor R_μ are defined based on eqs. (8) and (9), respectively.

$$R_\mu = V_e/V_y \tag{8}$$

$$\Omega = V_y/V_s \tag{9}$$

In these equations, V_s represents the shear corresponding to the formation of the first plastic hinge on the push-over curve of the

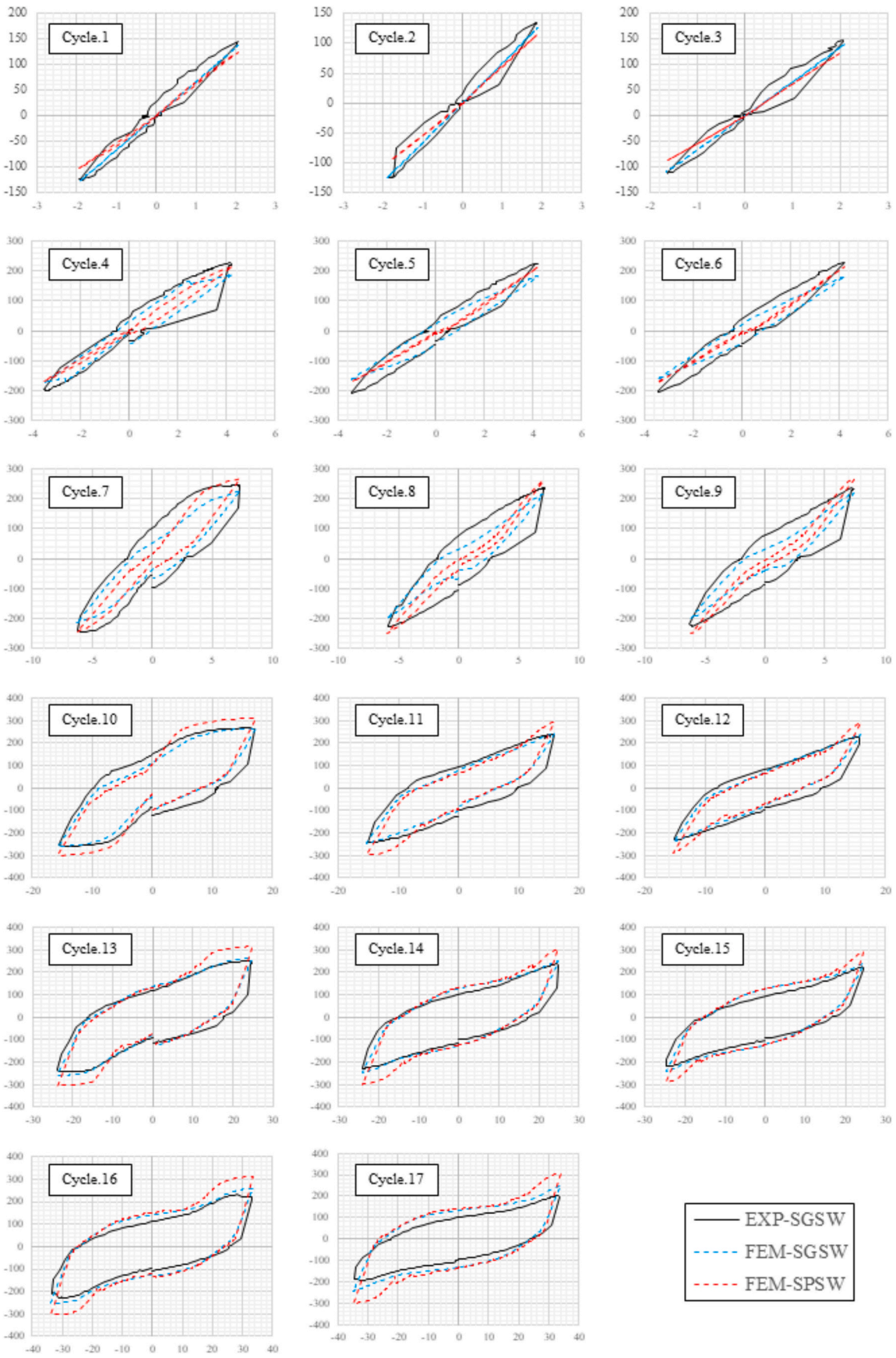

Fig. 18. The Cyclic comparison between EXP-SGSW, FEM-SGSW and SPSW.

Table 9
The energy dissipation comparison.

Load level	Number of cycles	SGSW	FEM-SGSW	FEM-SPSW
		kN.m	kN.m	kN.m
	1	0.12	0.00	0.01
$\Delta_y/3$	2	0.12	0.00	0.00
	3	0.11	0.00	0.00
	4	0.65	0.38	0.14
$2\Delta_y/3$	5	0.49	0.32	0.04
	6	0.48	0.29	0.04
	7	2.18	1.16	0.89
Δ_y	8	1.73	0.74	0.35
	9	1.75	0.75	0.35
	10	7.96	5.95	6.70
$2\Delta_y$	11	5.79	4.13	4.22
	12	4.85	3.68	3.37
	13	10.65	10.04	10.89
$3\Delta_y$	14	9.14	9.09	9.87
	15	8.13	8.81	9.34
$4\Delta_y$	16	13.54	15.22	16.98
	17	11.40	14.24	16.22
$5\Delta_y$*	18	6.58	9.98	11.34

S: represents the area enclosed by the hysteresis loop in each loading cycle, measured in kN·m, which indicates the energy dissipated by the specimen during that cycle.
* The final loading cycle corresponding to $5\Delta_y$ was not fully completed.

structure, V_y represents the shear corresponding to the yield point on the bilinear curve of the structure, and V_e corresponds to the shear force that the structure should withstand elastically without entering the nonlinear range. Therefore, the structural behavior factor can be calculated from Eq. (10).

$$R = R_\mu \Omega = V_e/V_y \times V_y/V_s = V_e/V_s \tag{10}$$

6.2.1. *Overstrength factor (Ω)*

To calculate the system overstrength factor, an idealized bilinear curve of the SGSW has been employed. To achieve this, the linear region of the bilinear curve has been extended to align with the area under the curve obtained from the idealized bilinear curve attained by FEMA-356 method [66]. As specified in this code, the bilinear and actual envelope curves intersect at 0.6Vy. Moreover, the area beneath the envelope curve and the bilinear curve are equal. Furthermore, the yielding point of the bilinear curve is always less than the maximum shear strength. Backbone curve of models are shown in Fig. 20. Based on the results presented in Table 10, the overstrength ratio of FEM-SPSW compared to FEM-SGSW is 22.28 % higher, and the overstrength ratio of FEM-SGSW compared to SGSW is 2.80 % higher. Fig. 21 demonstrates the comparison of the average overstrength ratios for the specimens.

6.2.2. *Ductility reduction factor* (R_μ)

As previously mentioned, the ductility reduction factor can be determined using eq. (8). This factor is crucial in assessing the structure's capacity to absorb and dissipate energy. The average ductility reduction factors for the specimens are shown in Fig. 21. Furthermore, Table 10 reveals that the ductility reduction factor of SGSW is 7.55 % greater than that of FEM-SGSW, while the ductility factor of FEM-SGSW is 13.59 % greater than that of FEM-SPSW.

6.2.3. *Structural ductility factor (μ)*

According to the equations provided by Uang [76], the ductility reduction factor can be calculated from Eq. (11).

$$\mu = \Delta_{max}/\Delta_y \tag{11}$$

Based on the results presented in Table 10, the ductility of SGSW is found to be 14.40 % higher compared to FEM-SGSW, while FEM-SGSW exhibits a 29.59 % higher ductility compared to FEM-SPSW. Additionally, the response modification factor for SPSW, SGSW, and FEM-SGSW are determined to be 8.07, 7.83, and 7.49, respectively, as revealed by the results presented in Table 10. Specifically, the response modification coefficient for SPSW is observed to be 3 % higher than that of SGSW. According to the provisions of AISC 341 [60] and FEMA 450 [78], the response modification factor (R) for conventional steel plate shear walls (SPSWs) is typically taken as 7. The close alignment of these values suggests that the proposed SGSW system demonstrates comparable seismic performance to conventional SPSWs. As mentioned earlier, the use of a steel mesh with an angle cross-section has led to an increase in

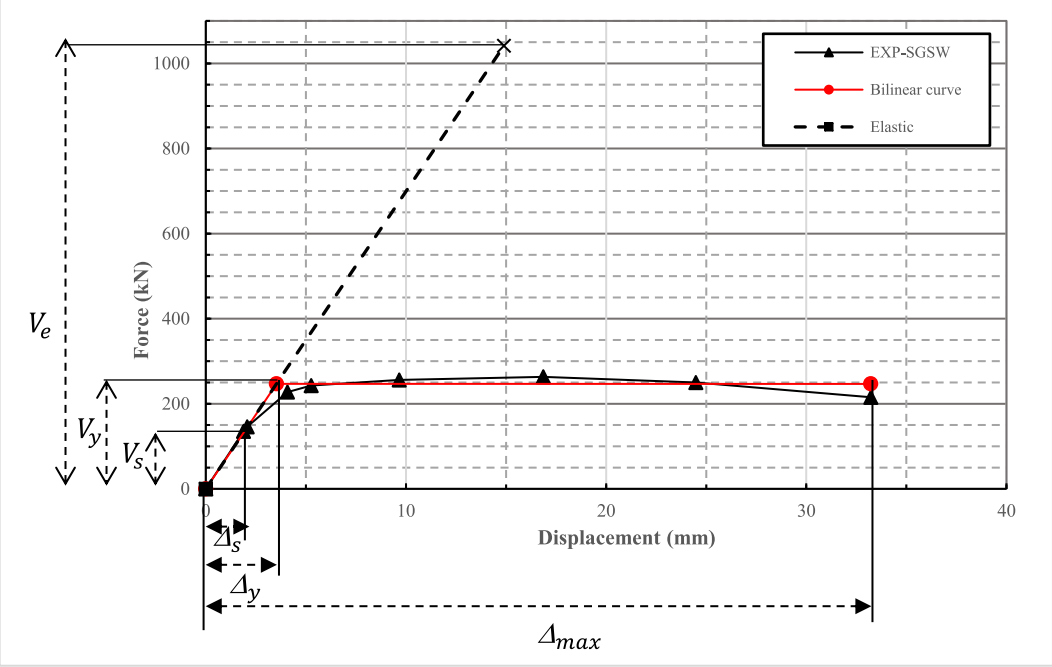

Fig. 19. General structural response.

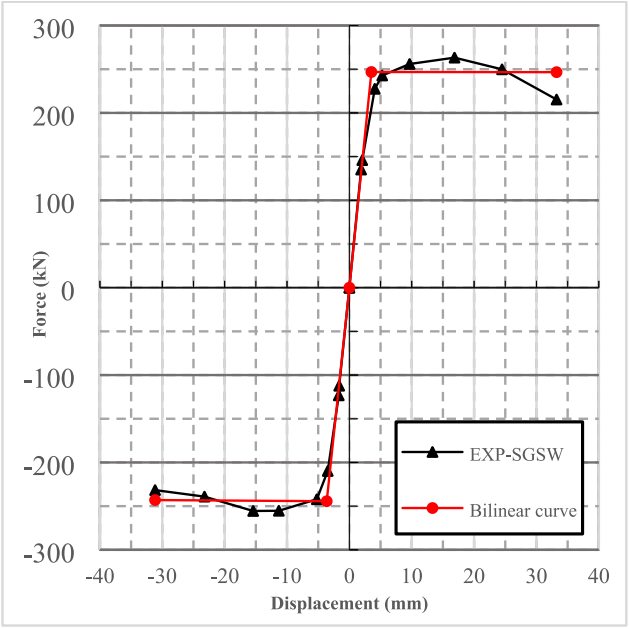

(a) Bilinear curve of EXP-SGSW.

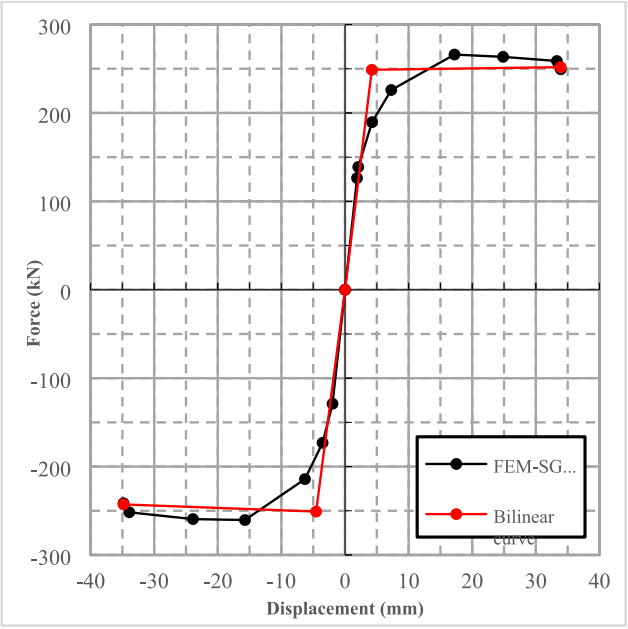

(b) Bilinear curve of FEM-SGSW.

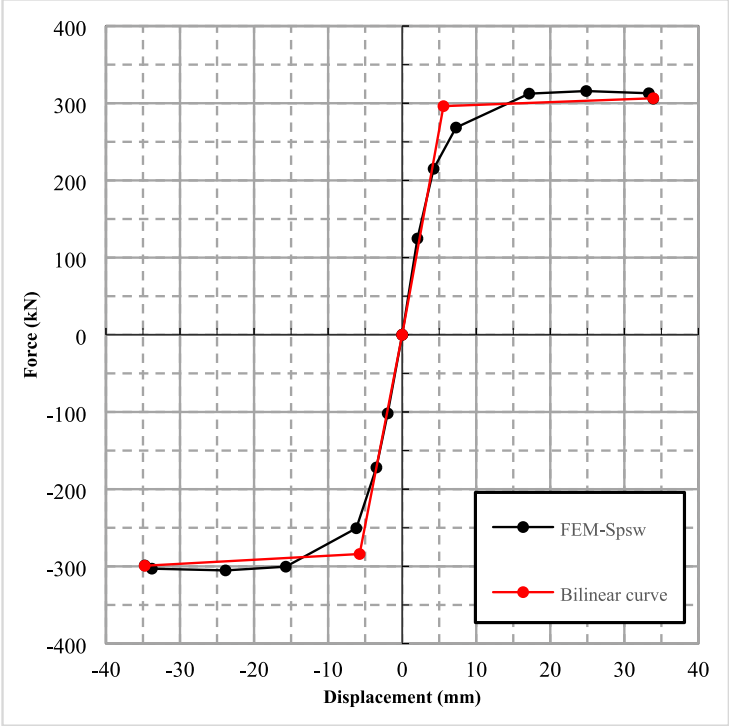

(c) Bilinear curve of FEM-SPSW.

Fig. 20. Idealized force-displacement curves.

the initial stiffness compared to a SPSW, resulting in an enhanced ductility ratio. However, due to the segmentation of the wall, the overstrength factor in this system has decreased. Ultimately, the response modification factor in both the SGSW and SPSW models was found to be the same. These findings indicate that the SGSW system can be considered a suitable alternative to traditional steel shear walls in various buildings.

In this study, due to limitations in laboratory space and equipment, the SGSW specimen was tested with dimensions of 1440 × 1130 mm. Additionally, this paper analyzes a height-to-width ratio of 1.3 for the SGSW. As such, it is strongly recommended that future research explore a wider range of frame aspect ratios and examine the influence of the length-to-thickness ratio of angle web elements on the seismic performance of SGSWs. Further comparisons with other modified systems, such as perforated SPSWs, and testing of large-scale specimens under cyclic loading would provide valuable insights. Moreover, it is important to recognize that the response modification factor (R) and overstrength factor (Ω) presented in this study were estimated using simplified procedures originally proposed by Uang [76], which serve as a preliminary basis for evaluation. In modern seismic design practice, determining codified values for R and Ω requires a comprehensive framework involving nonlinear dynamic analysis, collapse simulations under suites

Table 10
Comparision of response modification factor from SGSW and SPSW specimens.

Specimen	EXP-SGSW		FEM-SGSW		EXP-SGSW	
	Pull	Push	Pull	Push	Pull	Push
V_s (kN)	135.24	123.09	126.38	128.95	124.69	117.79
V_y (kN)	246.81	244.36	248.81	250.91	296.21	284.02
V_e (kN)	1041.64	980.23	969.97	942.73	997.59	957.64
K_e (kN/mm)	69.90	67.22	59.11	55.25	53.14	49.42
μ	9.41	8.58	8.06	7.67	6.08	6.05
R_μ	4.22	4.01	3.90	3.76	3.37	3.37
Ω	1.83	1.98	1.97	1.95	2.38	2.41
R	7.70	7.96	7.67	7.31	8.00	8.13
R_{mean}	7.83		7.49		8.07	

of ground motions, and probabilistic performance evaluation consistent with methodologies such as FEMA P695 [79]. Accordingly, the values reported herein should be interpreted as relative indicators of seismic behavior, pending future research that incorporates these advanced methods to formally validate the seismic design parameters of the SGSW system.

7. Conclusion

In this study, the lateral load performance of a novel Steel Grid Shear Wall (SGSW) under cyclic loading was investigated. For this purpose, an SGSW specimen was designed and tested under cyclic loading to evaluate the seismic behavior of this system. Subsequently a finite element model of the SGSW specimen was developed based on experimental results, and the accuracy of the modeling was validated. Additionally, the seismic performance of SGSW and SPSW was compared using finite element analysis. The results demonstrated that the SGSW system effectively can perform as an alternative to SPSW system. SGSW specially can address the limitations associated with steel plate shear walls (SPSWs) with very thin plates such as fire damageability and distortions during the construction procces. Finally, this study examined and discussed the structural characteristics of SGSW, including ultimate strength, initial stiffness, ductility, and energy dissipation capacity. The following conclusions were obtained

1. The experimental results of the SGSW confirmed the satisfactory performance of its yielding and failure processes. Under cyclic lateral loading, the steel grid members initially buckled and yielded gradually, and ultimately fractured after several cycles. As the lateral load increased, plastic hinges developed at both ends of the beam and eventually at the column bases. The SGSW exhibited stable hysteretic behavior, high ductility, significant shear strength, exceptional energy dissipation capacity, and elevated initial stiffness, highlighting its robustness for seismic applications.
2. The developed finite element model accurately simulates the behavior of the experimental SGSW specimen. The shape of the hysteresis curves for both the experimental and FEM specimen were similar, with the difference in maximum lateral load between the two being less than 1 %. Additionally, the differences in dissipated energy and initial stiffness were less than 6 % and 4 %, respectively
3. A numerical study using a finite element model was performed to compare the seismic behavior of SPSW and SGSW with equal weight. The results showed that the maximum lateral bearing capacity of the SGSW system was reduced by only 18 % compared to the traditional flat steel plate shear wall
4. Due to the out-of-plane stiffness of the angle sections the initial stiffness of SGSW has improved compared to the frame with an integrated steel plate. According to the numerical analysis results, the initial stiffness of the SGSW is 17.6 % higher than that of the SPSW with identical materials.
5. By comparing the hysteresis curves of SPSW and SGSW, it is observed that both systems exhibit stable hysteresis behavior and demonstrate similar energy dissipation capacities. The results indicate that the energy absorption capacity of the FEM-SGSW model is only 6 % lower than that of the FEM-SPSW model.
6. The increase in the initial stiffness of the system, and consequently the reduction in the displacement corresponding to the yield point of SGSW compared to SPSW, has resulted in a 29.59 % increase in the ductility factor of the SGSW system relative to the SPSW.

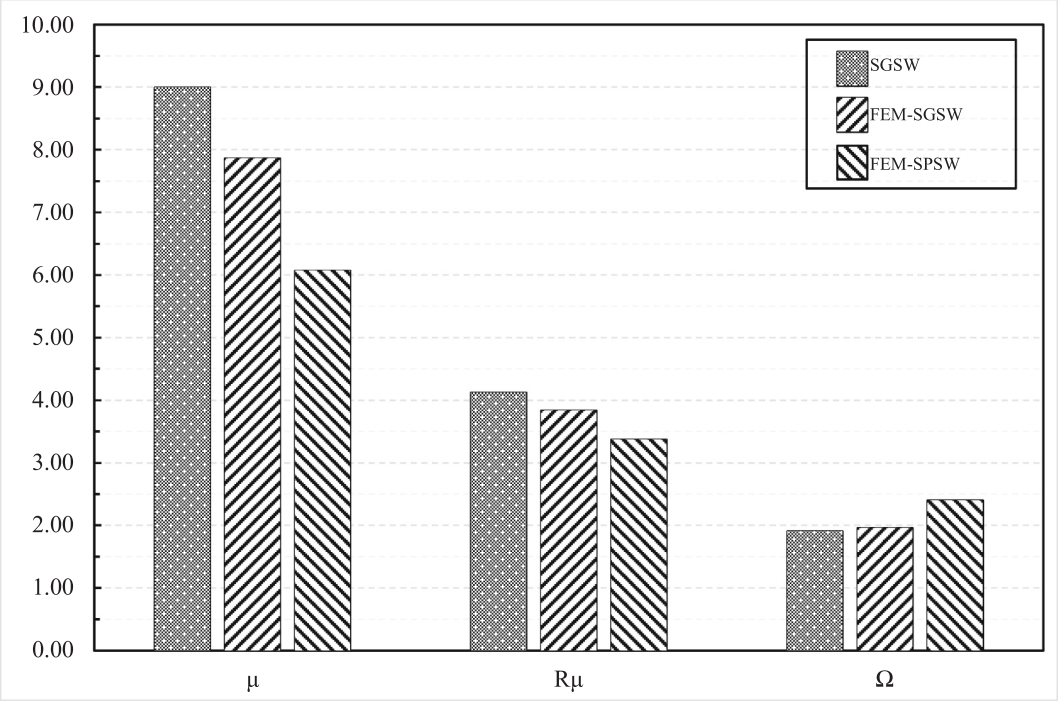

Fig. 21. Structural ductility factor, ductility reduction factor and overstrength factor of specimens.

7. Overstrength and ductility reduction factors were calculated utilizing the pushover curve derived from the hysteresis curves of experimental and numerical studies, The results demonstrated that the discretization of the continuous steel plate with steel grid bars resulted in an 18 % reduction in the overstrength factor of SGSW compared SPSW. Furthermore, the increase in stiffness, contributed to a 13.6 % rise in the ductility reduction factor. Finally, the results indicate that Response modification factor of SGSW is only 7.1 % lower than that of SPSW. Additionally, it was concluded that SGSWs can serve as a viable alternative to SPSWs, effectively addressing the challenges associated with traditional steel plate shear walls.

Despite the promising results obtained in this study, several limitations must be acknowledged. The experimental investigation was limited to a single-story, single-bay SGSW specimen, and the response under full-scale, multi-story conditions remains to be validated. Moreover, the estimated response modification factor (R) was derived using simplified formulations based on test results and not through comprehensive nonlinear dynamic analysis or collapse simulations. Additionally, constructability, cost-efficiency, and large-scale implementation aspects of the SGSW system were not investigated in detail. Future studies are therefore strongly recommended to extend the investigation to full-scale or multi-story SGSW systems, perform detailed pushover and time-history analyses, explore various grid geometries and connection details, and evaluate fabrication feasibility and cost compared to conventional SPSWs.

CRediT authorship contribution statement

Alireza Vatankhah: Writing – review & editing, Writing – original draft, Visualization, Validation, Methodology, Investigation, Conceptualization. **Abbas Karamodin:** Writing – review & editing, Supervision, Project administration, Conceptualization.

Funding sources

This research received no specific grant from any funding agency, commercial, or not-for-profit sectors.

Declaration of competing interest

The authors declare no conflicts of interest related to this work.

Acknowledgements

I sincerely thank my supervisor, Dr. Karamodin, for their invaluable guidance, encouragement, and insightful feedback throughout this research. Their expertise and support have been instrumental in shaping this work. I also appreciate the assistance and contributions of my colleagues in facilitating this study.

Data availability

All data generated or analyzed during this study are included in this published article. The raw data is also available from the corresponding author on reasonable request.

References

[1] Y. Takahashi, Y. Takemoto, T. Takeda, M. Takagi, Experimental study on thin steel shear walls and particular steel bracings under alternative horizontal load, in: IABSE Symp. Resist. Ultim. Deform. Struct. Acted by Well-Defined Repeated Loads, 1973, pp. 185–191, https://doi.org/10.5169/seals-13,766 [Online]. Available.
[2] R.G. Driver, G.L. Kulak, D.J.L. Kennedy, A.E. Elwi, Cyclic test of four-story steel plate shear wall, J. Struct. Eng. 124 (2) (1998) 112–120, https://doi.org/10.1061/(asce)0733-9445(1998)124:2(112).
[3] Q. Zhao, A. Astaneh-Asl, Cyclic behavior of an innovative steel shear wall system, in: Proceedings of the 13th World Conference on … 2576, 2004 [Online]. Available: http://www.iitk.ac.in/nicee/wcee/article/13_2576.pdf.
[4] M.R. Behbahanifard, Cyclic Behaviour of Unstiffened Steel Plate Shear Walls.pdf, University of Alberta, 2003.
[5] G.S. Sabouri, M. Ghol Haki, Ductility of thin steel plate shear walls, Asian J. Civil Eng. (Build. Hous.) 9 (2) (2008) 153–166.
[6] V. Caccese, M. Elgaaly, R. Chen, Study of thin steel-plate, J. Struct. Eng. 119 (2) (1993) 573–587.
[7] A.S. Lubell, Performance of Unstiffened Steel Plate Shear Walls under Cyclic Quasi-Static Loading, 1997.
[8] L.J. Thorburn, G.L. Kulak, Analysis of Steel Plate Shear Walls, The University of Alberta Edmonton, Alberta, 1983, https://doi.org/10.3850/978-981-08-6218-3_ss-we025.
[9] P.A. Timler, G.L. Kulak, Experimental study of steel plate shear walls, Struct. Eng. Rep. 114 (1983).
[10] J.J. Shishkin, R.G. Driver, G.Y. Grondin, Analysis of steel plate shear walls using the modified strip model, Struct. Eng. Rep. 261 (2009) 1–163, https://doi.org/10.1061/(asce)st.1943-541x.0000066.
[11] W. Tian, Y. Ma, J.W. Berman, Uniform strip model of steel plate shear walls with different plate thicknesses, J. Struct. Eng. 147 (11) (2021), https://doi.org/10.1061/(asce)st.1943-541x.0003134.
[12] J. Berman, M. Bruneau, Plastic analysis and design of steel plate shear walls, J. Struct. Eng. 129 (11) (2003) 1448–1456, https://doi.org/10.1061/(asce)0733-9445(2003)129:11(1448).
[13] S. Sabouri-Ghomi, S.R.A. Sajjadi, Experimental and theoretical studies of steel shear walls with and without stiffeners, J. Constr. Steel Res. 75 (2012) 152–159, https://doi.org/10.1016/j.jcsr.2012.03.018.
[14] J.-G. Nie, L. Zhu, J.-S. Fan, Y.L. Mo, Lateral resistance capacity of stiffened steel plate shear walls, Thin-Walled Struct. 67 (2013) 155–167, https://doi.org/10.1016/j.tws.2013.01.014.
[15] S. Sabouri-Ghomi, S. Mamazizi, Experimental investigation on stiffened steel plate shear walls with two rectangular openings, Thin-Walled Struct. 86 (2015) 56–66, https://doi.org/10.1016/j.tws.2014.10.005.
[16] H.C. Guo, J.P. Hao, Y.H. Liu, Behavior of stiffened and unstiffened steel plate shear walls considering joint properties, Thin-Walled Struct. 97 (2015) 53–62, https://doi.org/10.1016/j.tws.2015.09.005.
[17] H.C. Guo, Y.L. Li, G. Liang, Y.H. Liu, Experimental study of cross stiffened steel plate shear wall with semi-rigid connected frame, J. Constr. Steel Res. 135 (2017) 69–82, https://doi.org/10.1016/j.jcsr.2017.04.009.
[18] Z. Yong Ma, J. Ping Hao, H. Sheng Yu, Shaking-table test of a novel buckling-restrained multi-stiffened low-yield-point steel plate shear wall, J. Constr. Steel Res. 145 (2018) 128–136, https://doi.org/10.1016/j.jcsr.2018.02.009.
[19] Experimental and Numerical Investigations on Seismic Behavior of Hybrid.pdf, 2019.
[20] J.C. Cui, J.D. Xu, Z.R. Xu, T. Huo, Cyclic behavior study of high load-bearing capacity steel plate shear wall, J. Constr. Steel Res. 172 (2020), https://doi.org/10.1016/j.jcsr.2020.106178.
[21] Z. Cao, Z. Wang, P. Du, H. Liu, F. Fan, Quasi-static experiments on steel plate shear walls reinforced with X-shaped restrainers, J. Build. Eng. 31 (73) (2020) 101451, https://doi.org/10.1016/j.jobe.2020.101451.
[22] F. Aminifar, M.R. Sheidaii, S. Tariverdilo, Experimental investigation of parallel restrainers effects on buckling-restrained thin steel plate shear walls, J. Asian Architect. Build. Eng. 20 (6) (2021) 706–717, https://doi.org/10.1080/13467581.2020.1816548.
[23] J. Yu, F. Bu, B. Li, X. Feng, Seismic behaviour of steel plate shear wall with non-welded oblique multi-ribs, Structures 31 (2021) 1216–1229, https://doi.org/10.1016/j.istruc.2021.02.048.
[24] J.K. Tan, M.N. Su, Y.H. Wang, K. Wang, Y.Q. Cao, P. Li, Experimental study on cyclic shear performance of steel plate shear wall with different buckling restraints, Structures 35 (2022) 469–482, https://doi.org/10.1016/j.istruc.2021.11.021.
[25] K. Wang, et al., Lateral behaviour and failure modes of buckling-restrained beam-only-connected steel plate shear walls, Eng. Fail. Anal. 142 (2022), https://doi.org/10.1016/j.engfailanal.2022.106833.
[26] D. Vian, M. Asce, M. Bruneau, M. Asce, R. Purba, Special Perforated Steel Plate Shear Walls with Reduced.pdf no. March, ASCE, 2009, pp. 221–228.
[27] R. Purba, M. Bruneau, Finite-element investigation and design recommendations, J. Struct. Eng. 135 (2009) 1367–1376.
[28] H. Valizadeh, M. Sheidaii, H. Showkati, Experimental investigation on cyclic behavior of perforated steel plate shear walls, J. Constr. Steel Res. 70 (2012) 308–316, https://doi.org/10.1016/j.jcsr.2011.09.016.
[29] Z. Zhao, M. Zhang, Y. Gao, Q. Sun, Investigations on shear capacity of steel plates with local opening, J. Constr. Steel Res. 179 (2021), https://doi.org/10.1016/j.jcsr.2020.106518.
[30] S. Sabouri-Ghomi, E. Ahouri, R. Sajadi, M. Alavi, A. Roufegarinejad, M.A. Bradford, Stiffness and strength degradation of steel shear walls having an arbitrarily-located opening, J. Constr. Steel Res. 79 (2012) 91–100, https://doi.org/10.1016/j.jcsr.2012.07.017.
[31] N.A. Khan, G. Srivastava, Models for strength and stiffness of steel plate shear walls with openings, Structures 27 (2020) 2096–2113, https://doi.org/10.1016/j.istruc.2020.07.037.
[32] H. Valizadeh, B.F. Azar, H. Veladi, M.R. Sheidaii, The shear capacity assessment of steel plate shear walls with peripheral circular holes, Thin-Walled Struct. 163 (2021), https://doi.org/10.1016/j.tws.2021.107638.

[33] T.M. Roberts, S.S. Ghomi, Hysteretic characteristics of unstiffened plate shear panels, Thin-Walled Struct. 12 (2) (1992) 145–162, https://doi.org/10.1016/0263-8231(91)90061-M.
[34] M. Gorji Azandariani, M. Gholhaki, M.A. Kafi, Experimental and numerical investigation of low-yield-strength (LYS) steel plate shear walls under cyclic loading, Eng. Struct. 203 (2020), https://doi.org/10.1016/j.engstruct.2019.109866.
[35] M. Wang, H. Duan, G. Shi, Experimental study on seismic performance of low-yield point steel plate shear walls, Thin-Walled Struct. 191 (July) (2023) 111093, https://doi.org/10.1016/j.tws.2023.111093.
[36] J.W. Berman, M. Bruneau, Experimental investigation of light-gauge steel plate shear walls, J. Struct. Eng. 131 (7) (2005) 259–267, https://doi.org/10.1061/(asce)st.1943-541x.0000531.
[37] G. Cortés, J. Liu, Experimental evaluation of steel slit panelframes for seismic resistance, J. Constr. Steel Res. 67 (2) (2011) 181–191, https://doi.org/10.1016/j.jcsr.2010.08.002.
[38] J. Lu, S. Yu, J. Xia, X. Qiao, Y. Tang, Experimental study on the hysteretic behavior of steel plate shear wall with unequal length slits, J. Constr. Steel Res. 147 (2018) 477–487, https://doi.org/10.1016/j.jcsr.2018.05.002.
[39] W. Wang, J. Kong, Y. Zhang, G. Chu, Y. Chen, Seismic behavior of self-centering modular panel with slit steel plate shear walls: experimental testing, J. Struct. Eng. 144 (1) (2018) 1–13, https://doi.org/10.1061/(asce)st.1943-541x.0001932.
[40] G. Chu, W. Wang, Y. Zhang, Shake-table testing of 2-story steel framed building with self-centering modular panels and slit steel plate walls, Eng. Struct. 247 (April) (2021) 113232, https://doi.org/10.1016/j.engstruct.2021.113232.
[41] S. Heyrani Moghaddam, A. Shooshtari, Numerical and experimental investigation on seismic performance of proposed steel slit dampers, J. Constr. Steel Res. 200 (November 2022) (2023) 107646, https://doi.org/10.1016/j.jcsr.2022.107646.
[42] J. Hao, S. Li, W. Tian, X. Wu, Seismic performance of coupled steel plate shear wall with slits, J. Constr. Steel Res. 201 (2023), https://doi.org/10.1016/j.jcsr.2022.107674.
[43] B. Shekastehband, A.A. Azaraxsh, H. Showkati, Experimental seismic study on shear walls with fully-connected and beam-only-connected web plates, J. Constr. Steel Res. 141 (2018) 204–215, https://doi.org/10.1016/j.jcsr.2017.11.013.
[44] N. Paslar, A. Farzampour, F. Hatami, Infill plate interconnection effects on the structural behavior of steel plate shear walls, Thin-Walled Struct. 149 (2020), https://doi.org/10.1016/j.tws.2020.106621.
[45] D.H. Shin, H.J. Kim, Post-buckling strengths of steel-plate shear walls with two-side clamped boundary conditions, Thin-Walled Struct. 170 (2022), https://doi.org/10.1016/j.tws.2021.108499.
[46] M.W. Wei, J.Y. Richard Liew, D. Yong, X.Y. Fu, Experimental and numerical investigation of novel partially connected steel plate shear walls, J. Constr. Steel Res. 132 (2017) 1–15, https://doi.org/10.1016/j.jcsr.2017.01.013.
[47] M. Kurata, R.T. Leon, R. Desroches, M. Nakashima, Steel plate shear wall with tension-bracing for seismic rehabilitation of steel frames, J. Constr. Steel Res. 71 (2012) 92–103, https://doi.org/10.1016/j.jcsr.2011.10.026.
[48] N. Egorova, M.R. Eatherton, A. Maurya, Experimental study of ring-shaped steel plate shear walls, J. Constr. Steel Res. 103 (2014) 179–289.
[49] A.R. Phillips, M.R. Eatherton, Large-scale experimental study of ring shaped–steel plate shear walls, J. Struct. Eng. 144 (8) (2018), https://doi.org/10.1061/(asce)st.1943-541x.0002119.
[50] S. Kordbegli, A. Haghollahi, F. Farahbod, Seismic behavior of a novel RSSC-SPSW: an experimental and numerical study, J. Constr. Steel Res. 196 (2022), https://doi.org/10.1016/j.jcsr.2022.107376.
[51] J. Wang, Y. Zhu, X. Cai, Y. Wen, P. Wang, Hysteresis behavior of auxetic perforated steel plate shear walls with elliptical and peanut-shaped cutouts, J. Build. Eng. 79 (July) (2023) 107875, https://doi.org/10.1016/j.jobe.2023.107875.
[52] H. Monsef Ahmadi, M.R. Sheidaii, H. Boudaghi, G. De Matteis, Experimental and numerical study on largely perforated steel shear plates with rectangular tube–shaped links, Adv. Struct. Eng. 23 (15) (2020) 3307–3322, https://doi.org/10.1177/1369433220937147.
[53] H. Arash Akbari, R. Barzegar Asl, H. Rahimzadeh, Experimental and numerical study on the structural performance of auxetic-shaped, ring-shaped and unstiffened steel plate shear walls, J. Build. Eng. 34 (2021).
[54] A.R. Phillips, M.R. Eatherton, Computational study of elastic and inelastic ring shaped – steel plate shear wall behavior, Eng. Struct. 177 (June) (2018) 655–667, https://doi.org/10.1016/j.engstruct.2018.10.008.
[55] Y. Yang, X. Yan, Z. Chen, Y. Wen, Theoretical and parametric studies on the lateral-resistant performance of the steel grid shear wall, Buildings 15 (7) (2025) 1099, https://doi.org/10.3390/buildings15071099.
[56] X. Yan, Y. Yu, M. Zhang, Research on performance-based seismic design method of steel grid wall, Prog. Steel Build. Struct. (2024) 1–10.
[57] Z. Chen, Y. Yang, X. Yan, Y. Duan, T. Zhang, J. Wang, Cyclic tests and parametric analyses of steel grid shear walls, J. Constr. Steel Res. 200 (November 2022) (2023) 107647, https://doi.org/10.1016/j.jcsr.2022.107647.
[58] J. Guang Yu, T. Yi Zhang, C. Zhao, B. Li, Seismic behavior of self-restrained grid shear wall with diagonal CFRP-steel composite strips, J. Constr. Steel Res. 212 (July 2023) (2024), https://doi.org/10.1016/j.jcsr.2023.108216.
[59] A. Vatankhah, Investigating the Effect of Using Equivalent Sections as Axial Elements in the Strip Model of a Steel Plate Shear Wall System, Master's thesis, Ferdowsi University of Mashhad, 2023.
[60] AISC 341--16, Seismic Provision for Strucural Steel Building, American Institute of Steel Construction, 2016.
[61] Steel Design Guide 20, Steel Plate Shear Walls, American Institute of Steel Construction, 2007.
[62] A. 360--22, American Institute of Steel Construction, ANSI/AISC 360-22: Specification for Structural Steel Buildings, AISC, Chicago, IL, USA, 2022.
[63] Deutsches Institut für Normung, DIN 17100: Steels for General Structural Purposes, German Institute for Standardization (DIN), Berlin, Germany, 1980.
[64] American Society for Testing and Materials, ASTM E8/E8M: Standard Test Methods for Tension Testing of Metallic Materials no. 08.01, Book of ASTM Standards, 2022, p. 31 [Online]. Available: www.astm.org.
[65] ATC-24, Guidelines for Seismic Testing of Components of Steel Structures, Applied Technology Council, 1992.
[66] Fema 356, NEHRP Commentary on the Guidelines for the Seismic Rehabilitation of Buildings October, Fed. Emerg. Manag. Agency, Washington, DC, Dev. by Appl. Technol. Counc., 1997, pp. 1–518.
[67] X. Zhang, et al., Investigation on hysteretic performance of assembled H-shaped steel frame-corrugated steel plate shear wall with different corrugated orientation and wavelength, J. Build. Eng. 77 (August) (2023) 107473, https://doi.org/10.1016/j.jobe.2023.107473.
[68] J.L. Chaboche, Constitutive equations for cyclic plasticity and cyclic viscoplasticity, Int. J. Plast. 5 (3) (1989) 247–302, https://doi.org/10.1016/0749-6419(89)90015-6.
[69] J.L. Chaboche, Time-independent constitutive theories for cyclic plasticity, Int. J. Plast. 2 (2) (1986) 149–188, https://doi.org/10.1016/0749-6419(86)90010-0.
[70] S. Jin, J. Bai, J. Ou, Seismic behavior of a buckling-restrained steel plate shear wall with inclined slots, J. Constr. Steel Res. 129 (2017) 1–11, https://doi.org/10.1016/j.jcsr.2016.10.005.
[71] M. Wang, Y. Shi, J. Xu, W. Yang, Y. Li, Experimental and numerical study of unstiffened steel plate shear wall structures, J. Constr. Steel Res. 112 (2015) 373–386, https://doi.org/10.1016/j.jcsr.2015.05.002.
[72] H. Hibbitt, B. Karlsson, P. Sorensen, ABAQUS Analysis Users Manual Version 6.6, 2006.
[73] European Committee for Standardization (CEN), Eurocode 3: Design of Steel Structures—Part 1-5: Plated Structural Elements, EN 1993-1-5:2006, Brussels, Belgium, 2006.
[74] European Committee for Standardization (CEN), Eurocode 3: Design of Steel Structures—Part 1-1: General Rules and Rules for Buildings, EN 1993-1-1:2005, Brussels, Belgium, 2005.
[75] Building Seismic Safety Council and United States, Federal Emergency Management Agency, NEHRP Recommended Provisions for the Development of Seismic Regulations for New Buildings, FEMA, 1988.
[76] C.M. Uang, Establishing R (or Rw) and Cd factors for building seismic provisions, J. Struct. Eng. 117 (1) (1991) 19–28.
[77] Michael Smith, ABAQUS/Standard User's Manual, Version 6.9, Dassault Systemes Simulia Corp, United States, 2009.
[78] Federal Emergency Management Agency (FEMA), Recommended Provisions for Seismic Regulations for New Buildings and Other Structures(FEMA 450). Washington, DC, 2003.
[79] Federal Emergency Management Agency, Quantification of Building Seismic Performance Factors (FEMA P-695), Federal Emergency Management Agency, Washington, DC, 2009 [Online]. Available: https://www.fema.gov/sites/default/files/2020-07/fema_p695.pdf.